

Bias Field Correction for Retinal Perfusion Heterogeneity Analysis of Optical Coherence Tomography Angiography

**by
Henry Hodaly**

Thesis Submitted in Partial Fulfillment of the
Requirements for the Degree of
Bachelor of Applied Science

in the
School of Engineering Science

**© Henry Hodaly 2023
SIMON FRASER UNIVERSITY
Spring 2023**

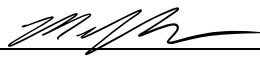
Copyright in this work is held by the author. Please ensure that any reproduction or re-use is done in accordance with the relevant national copyright legislation.

APPROVAL

Name: Henry Hodaly

Degree: Bachelor of Applied Science Honours

Title of Thesis: Bias Field Correction for Retinal Perfusion Heterogeneity Analysis of Optical Coherence Tomography Angiography

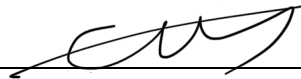


Dr. Michael Sjoerdsma, P.Eng.
Acting Director, School of Engineering Science


Examining Committee:



Dr. Marinko Sarunic, P.Eng.
Professor, School of Engineering Science



Dr. Myeong Jin Ju
Assistant Professor, UBC

Mirza Faisal Beg  Digitally signed by Mirza Faisal Beg
DN: cn=Mirza Faisal Beg, o=Simon Fraser University, ou=School of
Engineering Science, email=mbeg@sfu.ca, c=US
Date: 2023.04.21 02:47:00 -07'00'

Dr. Mirza Faisal Beg, P.Eng.
Professor, School of Engineering Science

Date Approved:

April 20, 2023

Abstract

In this thesis, a method for bias field correction is proposed for Optical Coherence Tomography Angiography (OCT-A) images. The bias field artifact is an intensity nonuniformity present on OCT-A images caused by inaccuracies during image acquisition. The OCT volumetric data is used to estimate bias produced due to the tilt of the retina. Bias field correction will occur prior to a 2-D registration algorithm used to correct for micro-saccadic motion and construct a clear, high-quality image of the retina for retinal perfusion heterogeneity analysis.

Acknowledgements

I would like to begin by expressing my sincere gratitude to Dr. Marinko Sarunic for his guidance and patience throughout my thesis. His knowledge and expertise in this field were crucial as I undertook this journey and his feedback was thoughtful. He inspired and encouraged me to find new ways to interpret the data and continually challenge myself.

I would also like to express my gratitude and appreciation to Dr. Myeong Jin Ju for his time and support. Having someone with his knowledge and experience to talk to weekly provided invaluable guidance and allowed me to maintain forward momentum when I encountered obstacles. I am also grateful to Dr. Mirza Faisal Beg who gave me my first opportunity to work with image processing and sparked my interest in this field.

In addition, I would like to send a special thank you to Arman Athwal, Sherry Han and all the other members of the BORG Lab. It was a pleasure to work with such a kind and professional group of individuals that immediately made me feel welcome and part of their team.

Finally, a special thanks to my family and friends who have been there for me for years, providing love and support as I worked towards completing my undergraduate degree.

Table of Contents

Approval	ii
Abstract	iii
Acknowledgements	iv
List of Figures	vii
List of Tables	ix
List of Acronyms	x
Chapter 1: Introduction	1
1.1 Glaucoma and Diabetic Retinopathy	1
1.2 Optical Coherence Tomography	2
1.3 Optical Coherence Tomography Angiography	3
1.4 Bias Field Correction	4
1.5 Thesis Organization	4
Chapter 2: OCT-A Image Registration and Averaging Algorithm	5
2.1 Data Acquisition	6
2.2 Motion Detection	6
2.3 Registration and Averaging	6
2.4 Vessel Segmentation	8
2.5 Coefficient of Variation	10
2.6 Summary	11
Chapter 3: Methods for Bias Field Correction	12
3.1 Bias Field Engineering Design Specifications	12
3.2 Bias Field Design Overview	12
3.3 Bias Field Correction Using the En-Face OCT-A Images Produced by the Zeiss Plex Elite 9000	13
3.4 Bias Field Correction Using En-Face Images Produced from the Raw OCT-A Volume Data	14
3.5 Changes to CoV Map Visualization	25
3.6 Bias Field Correction Pipeline Flowchart	26
3.7 Summary	26

Chapter 4: Results	27
4.1 Visual Comparison of Uncorrected vs. Bias-Corrected OCT-A Images	27
4.2 Quantitative Comparison of Uncorrected vs. Bias-Corrected OCT-A Images.....	31
4.3 CoV Map Comparisons.....	32
4.4 Summary	33
Chapter 5: Conclusion	34
5.1 Discussion	34
5.1 Limitations and Future Work.....	34
References.....	36

List of Figures

Figure 1: Images illustrating the vision seen in people with (A) normal vision, (B) diabetic retinopathy, and (C) glaucoma [7]. 1

Figure 2: OCT B-scan of a healthy retina [10]..... 2

Figure 3: OCT volume of the retina [11]..... 2

Figure 4: OCT-A 3x3 mm images of the foveal region of the retina with motion artifacts identified. (A) Artifacts appear as bright white lines [16]. (B) Lateral shift artifacts indicated by the sharp discontinuity in the major blood vessels. 3

Figure 5: (A) OCT-A 3x3 mm of the foveal region of the retina. (B) Bias field artifact of (A) seen with a Gaussian filter [21]. The bias field can be seen as a smooth variation of intensities across an image..... 4

Figure 6: Registration and averaging pipeline flowchart. The red box indicates the new preprocessing step to be included, bias field correction..... 5

Figure 7: Figure 4 OCT-A subdivided into strips for registration with the removal of motion artifacts..... 7

Figure 8: (A) Strip overlaid with the template prior to registration. (B) Strip overlaid with the template after all registration is complete. Green and magenta indicate vessel misalignment while white indicates correct alignment..... 8

Figure 9: (A) A single OCT-A image with motion artifacts visible. (B) The result of 16 registered images averaged together, producing a high-quality image with clear vessels. (C) The averaged image (B) vessel segmented using a DNN..... 9

Figure 10: (A) An excellent quality CoV map. (B) A poor quality CoV map with a black region and vertical strip of colour variation highlighted. The color bar indicates the variation from dark blue through to red..... 10

Figure 11: Bias field correction using OCT-A images. (A) Original OCT-A 3x3 mm image acquired from the ZEISS PLEX Elite 9000. (B) Bias field artifact of (A) seen with a Gaussian filter [21]. (C) Corrected OCT-A image with the bias field removed. (D) Overlay of (A) and (C) visualizing the intensity differences after the bias field is removed..... 14

Figure 12: (A) Fast-scan B-scan of the OCT volume. (B) Slow-scan B-scan of the OCT volume. (C) Mean en-face projection of the OCT volume..... 15

Figure 13: OCT B-scan before (A) and after (B) 3-D bounded variance smoothing..... 16

Figure 14: Retinal layer subdivisions on an OCT B-scan..... 16

Figure 15: Shadow regions shown in the red boxes can decrease the intensity of the A-scan position, so a linear polynomial approximation was selected to minimize this affect..... 17

Figure 16: (A) Fast-scan view and (B) slow-scan view showing the BM and shifted BM segmentation boundaries..... 18

Figure 17: Shifted segmentation of the BM overlaid on (A) an OCT B-scan and (B) an OCT-A B-scan. (C) OCT-A en-face image produced from the averaged intensity values in the axial direction between the layers shown in (B). 19

Figure 18: (A) Fast-scan averaged intensity plot and linear polynomial approximation. (B) Slow-scan averaged intensity plot and linear polynomial approximation. 20

Figure 19: (A) Rotated fast-scan and (B) slow scan bias field estimations from the polynomial approximations in Figure 18. 21

Figure 20: A rotated single en-face image normalized (A) before bias correction and (B) after bias correction using Equation-(2). (C) Intensity difference of (A)-(B). 22

Figure 21: Comparison between the result of the DNN for vessel segmentation on (A) the 2-D OCT-A image from the Zeiss device and (B) the OCT-A image produced from the volume..... 23

Figure 22: CoV map with the inclusion of the background component. 24

Figure 23: Averaged en-face OCT-A image from (A) the 2-D Zeiss data and (B) the 3-D volume data. (C) The overlay between (A)and (B) ensuring pixel to pixel correspondence. 24

Figure 24: Grayscale visualization of the CoV values. The red box contains the maximum CoV value, while the green box indicates the suggested region to select the maximum CoV value from..... 25

Figure 25: Bias field correction pipeline flowchart. 26

Figure 26: Column (A) showcases a single image before and after bias correction for Subject 1 OD, a male with NTG. Column (B) showcases the averaged images before and after bias correction. 28

Figure 27: CoV maps for Subject 1 (A) before bias correction and (B) after bias correction..... 28

Figure 28: Column (A) showcases a single image before and after bias correction for Subject 2 OS, a male with POAG. Column (B) showcases the averaged images before and after bias correction. 29

Figure 29: CoV maps for Subject 2 (A) before bias correction and (B) after bias correction..... 29

Figure 30: Column (A) showcases a single image before and after bias correction for Subject 3 OD, a healthy male. Column (B) showcases the averaged images before and after bias correction. 30

Figure 31: CoV maps for Subject 3 (A) before bias correction and (B) after bias correction..... 30

Figure 32: CoV map depicting regions for calculation boundaries. 31

Figure 33: CoV maps of (A) Subject 1, (B) Subject 2 and (C) Subject 3 after bias correction using the visualization method discussed in Section 3.5..... 32

List of Tables

Table 1: CoV calculations before and after bias correction..... 31

List of Acronyms

2-D	Two Dimensional
3-D	Three Dimensional
BRISK	Binary Robust Invariant Scalable Keypoints
CoV	Coefficient of Variation
DM	Diabetes Mellitus
DNN	Deep Neural Network
DR	Diabetic Retinopathy
NPDR	Non-Proliferative Diabetic Retinopathy
PDR	Proliferative Diabetic Retinopathy
FA	Fluorescein Angiography
FAZ	Foveal Avascular Zone
IOP	Intraocular Pressure
NTG	Normal Tension Glaucoma
OAG	Open-Angle Glaucoma
OCT	Optical Coherence Tomography
OCT-A	Optical Coherence Tomography Angiography
SURF	Speeded-Up Robust Features

Chapter 1: Introduction

1.1 Glaucoma and Diabetic Retinopathy

Vision is the primary sensory modality that humans use in all aspects of their daily lives. A loss of vision caused by retinal diseases such as glaucoma and diabetic retinopathy results in a severely decreased quality of life for these people. Glaucoma is a group of progressive eye diseases often associated with changes in the intraocular pressure (IOP), which results in damage to the retina and optic nerve [1, 2]. It is a leading cause of irreversible blindness worldwide and it is estimated that the number of people diagnosed with glaucoma will reach 111.8 million by 2040 [2]. The two main classifications are known as primary and secondary glaucoma, with both containing subcategories known as open-angle and closed-angle glaucoma. Glaucoma is classified as primary when it appears without any underlying disease, while secondary glaucoma occurs because of trauma or an existing medical condition. In open-angle glaucoma, the IOP increases gradually and there is no pain, while closed-angled glaucoma can occur suddenly and cause immediate negative reactions. There is also open-angle Normal Tension Glaucoma (NTG), where the IOP has not deviated from the normal range yet damage to the optic nerve still occurs [2].

Many people with diabetes mellitus (DM) can develop diabetic retinopathy (DR), which is vision loss associated with damage to the retinal microvasculature due to high blood sugar levels [3]. It is estimated that the number of adults with DR around the world will increase from 103.12 million in 2020 to 160.5 million in 2045 [4]. DR is a leading cause of blindness in the adult working age population and can lead to other complications if left untreated [4, 5]. DR can be classified into two categories, the non-proliferative DR stage (NPDR) and the proliferative DR stage (PDR) [5]. The NPDR stage is characterised by changes in the microvasculature of the retina, resulting in bleeding and fluid leakage (macular edema). This causes vision distortion and if left untreated, DR in the NPDR stage can progress to the PDR stage. The PDR stage is associated with the formation of new, abnormal blood vessels in the retina. These blood vessels have weak walls and can leak into the vitreous, causing partial or complete blindness. The clinical examination of retinal blood flow is known as ophthalmic Fluorescein Angiography (FA) [6]. This procedure involves the injection of a dye contrast agent into the bloodstream, which will then highlight the microvasculature of the retina and allow for a diagnosis and continued monitoring of the DR disease progress. Although both glaucoma and DR are currently incurable, early detection and regular vision exams can slow the progression of vision loss. Figure 1 provides a visualization of how glaucoma and DR affects an individual's vision.

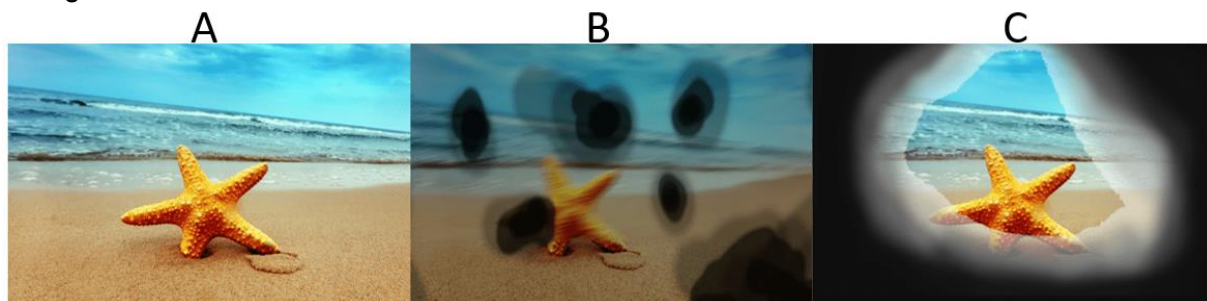


Figure 1: Images illustrating the vision seen in people with (A) normal vision, (B) diabetic retinopathy, and (C) glaucoma [7].

1.2 Optical Coherence Tomography

Optical Coherence Tomography (OCT) is an imaging procedure that uses light to acquire cross-sectional images of the retina *in-vivo* [8, 9]. OCT imaging allows clinicians to distinctly view the layers within the retina for the diagnosis of various diseases. This technique uses low powered laser light, is non-invasive and painless, therefore providing no risk of damage to the eye. The OCT imaging modality uses the concept of low coherence interferometry. A cross sectional depth profile of the imaged tissue layers is created by interfering a sample's backscattered light with a reference reflection generated from a path of known length. Axial cross-sectional data (A-scan) is acquired repeatedly while scanning transversely to acquire a brightness-scan (B-scan). A single B-scan visualizes a cross-sectional slice of the retina. Multiple B-scans taken in the direction perpendicular to the B-scan axis in a pre-determined pattern are then acquired to create a high-resolution, three-dimensional (3-D) OCT volume of the retina. Figure 2 provides an example of an OCT B-scan while Figure 3 provides a visualization of an OCT volume.

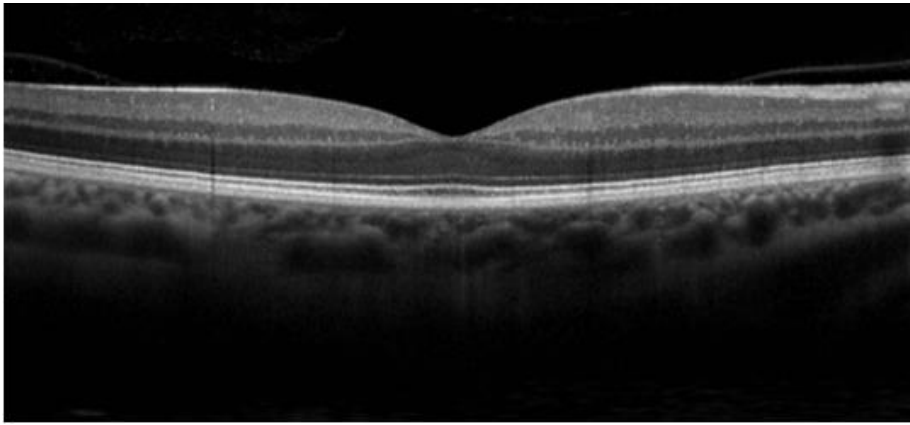


Figure 2: OCT B-scan of a healthy retina [10].

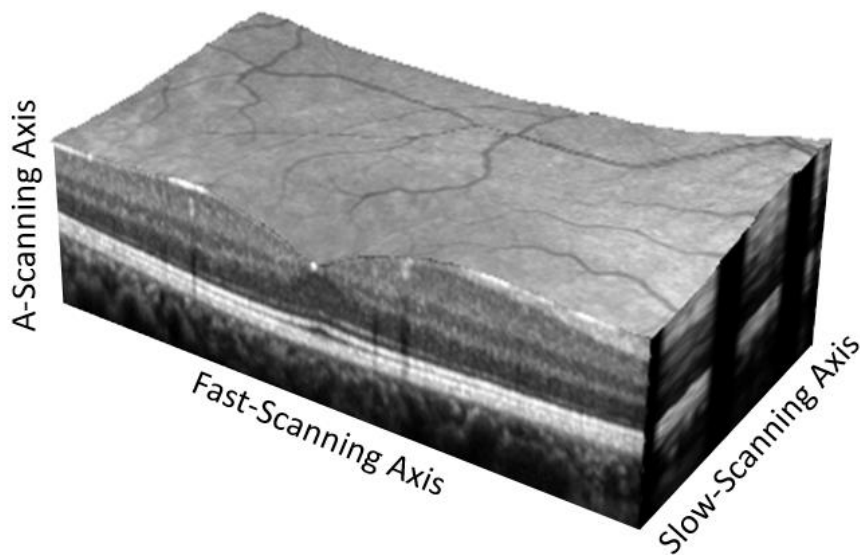


Figure 3: OCT volume of the retina [11].

1.3 Optical Coherence Tomography Angiography

Optical Coherence Tomography Angiography (OCT-A) is a technique utilizing OCT that allows for visualization of the retinal microvasculature without the need for a dye contrast agent, providing an advantage over FA [12-14]. Additionally, OCT-A provides a higher resolution and can differentiate between vascular layers within the retina, allowing for the study of the superficial, intermediate, and deep capillary plexuses [12, 13]. An OCT-A volumetric angiogram is acquired by collecting B-scans at the same position over a constant time interval, and then comparing the sequential scans to generate contrast based on the movement of blood [12-14]. Vessel locations that have a large variation of blood flow will result in high pixel intensity values on the OCT-A image, while locations that have minimal variation will have lower intensity pixels. This variation in blood flow can be used to analyze the microvasculature changes occurring throughout the layers of the retina and can be an indicator of DR and other diseases [12-15]. The foveal avascular zone (FAZ) is the smaller, central region of the fovea, the section of the retina with the highest visual acuity. The FAZ is devoid of blood vessels and will often exhibit disease features in OCT-A images.

The main drawback of OCT-A as opposed to FA is that OCT-A can suffer from motion artifacts, which can occur when a patient moves during the scanning procedure or from microsaccadic eye movements [12]. These motion artifacts can render data unusable. Figure 4 provides examples of OCT-A images with motion artifacts. A novel software algorithm comprising serial imaging, registration and averaging has been implemented to rectify the motion artifacts in the collected OCT-A data and construct a clear visualization of the retinal structures [16-19].

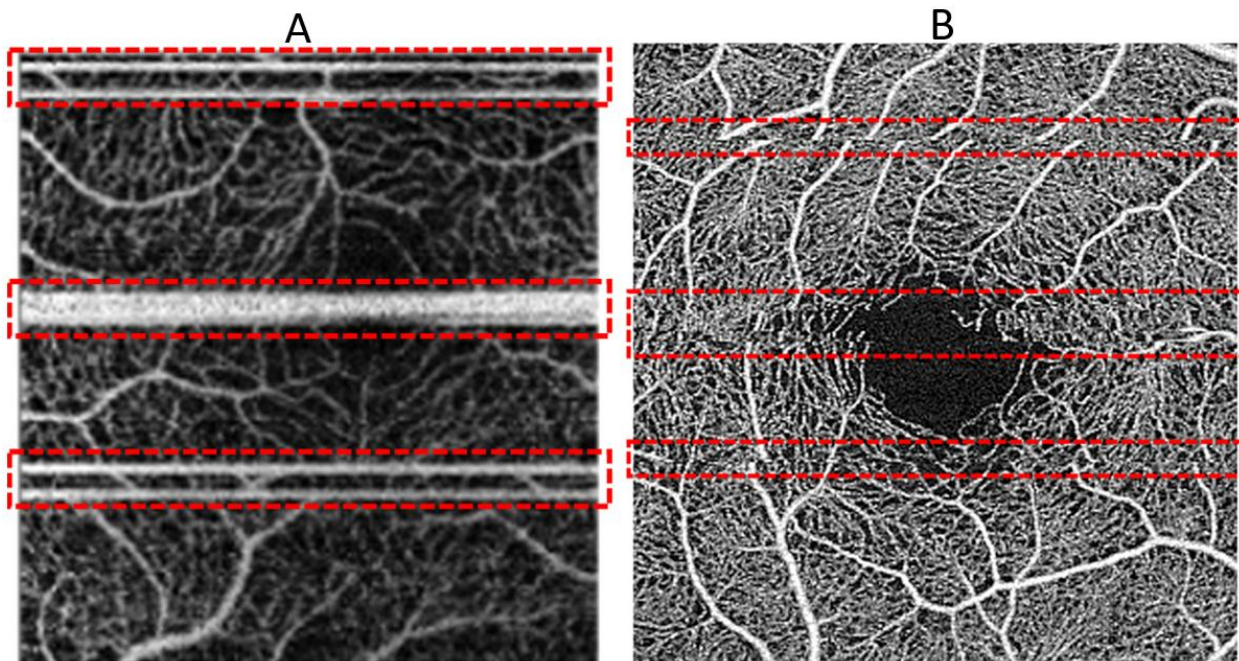


Figure 4: OCT-A 3x3 mm images of the foveal region of the retina with motion artifacts identified. (A) Artifacts appear as bright white lines [16]. (B) Lateral shift artifacts indicated by the sharp discontinuity in the major blood vessels.

1.4 Bias Field Correction

When an OCT-A image is acquired, there can be variations in image intensity due to flaws with the image acquisition process, such as incorrect focus or scan misalignment [20]. This low spatial frequency intensity inhomogeneity is known as a bias field and can degrade image quality, resulting in some structures or sections within an image appearing brighter than others. Figure 5 visualizes the bias field from a 3x3 mm OCT-A image.

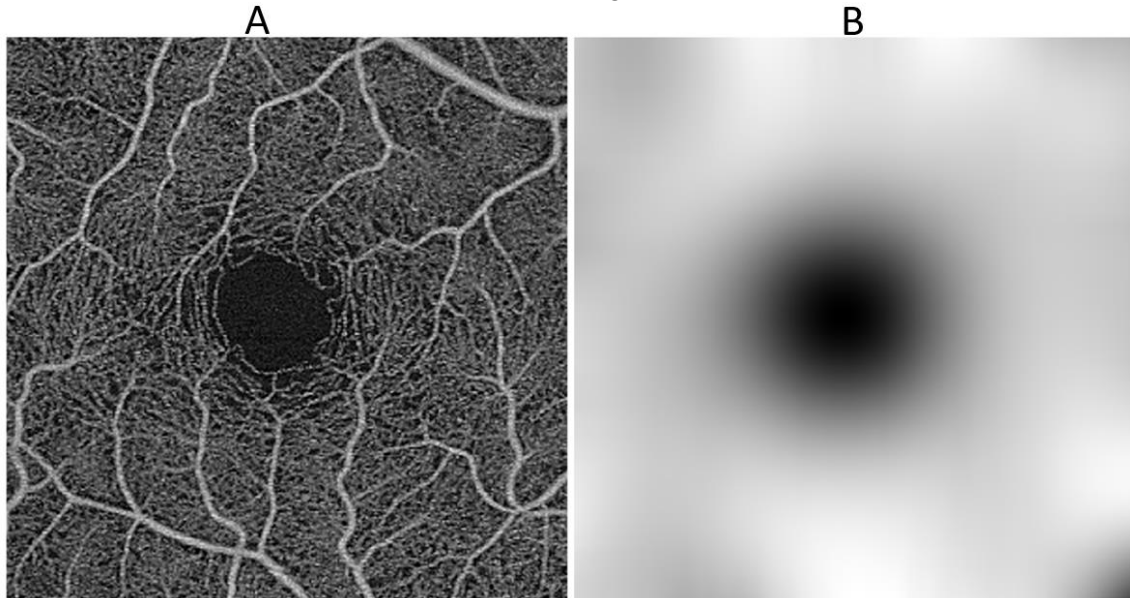


Figure 5: (A) OCT-A 3x3 mm of the foveal region of the retina. (B) Bias field artifact of (A) seen with a Gaussian filter [21]. The bias field can be seen as a smooth variation of intensities across an image.

The bias field intensity gradient artifact may influence the results of future analysis on the OCT-A images and needs to be removed, a process known as bias field correction [20-22]. Methods exist that perform bias field correction on magnetic resonance images [23-25], and this thesis aims to produce a similar algorithm to remove the bias field on OCT-A images. The objective of this thesis is to remove the bias field artifact from the OCT-A images before they are sent through the registration and averaging algorithm and then examine the effects observed when performing retinal perfusion heterogeneity analysis.

1.5 Thesis Organization

This thesis is organized into five chapters. Chapter 1 provides an introduction to retinal diseases, OCT and OCT-A imaging procedures, as well as the purpose of this thesis. Chapter 2 provides an overview of the registration and averaging algorithm used to quantify the perfusion heterogeneity with OCT-A images. Chapter 3 describes the various methods used for estimation and correction of the bias field in OCT-A images. The engineering design specifications are discussed in Section 3.1. Chapter 4 examines the results of bias field correction on the retinal perfusion heterogeneity analysis. Chapter 5 concludes this thesis with a summary and suggestions for related future work.

Chapter 2: OCT-A Image Registration and Averaging Algorithm

This chapter begins with a description of the data acquisition process and then explores the registration and averaging algorithm used to create a high-quality visualization of the retinal microvasculature. The chapter concludes with an explanation on how this algorithm is then used to examine the variation in blood flow in the retina. An overview of the algorithm is shown in the flowchart in Figure 6.

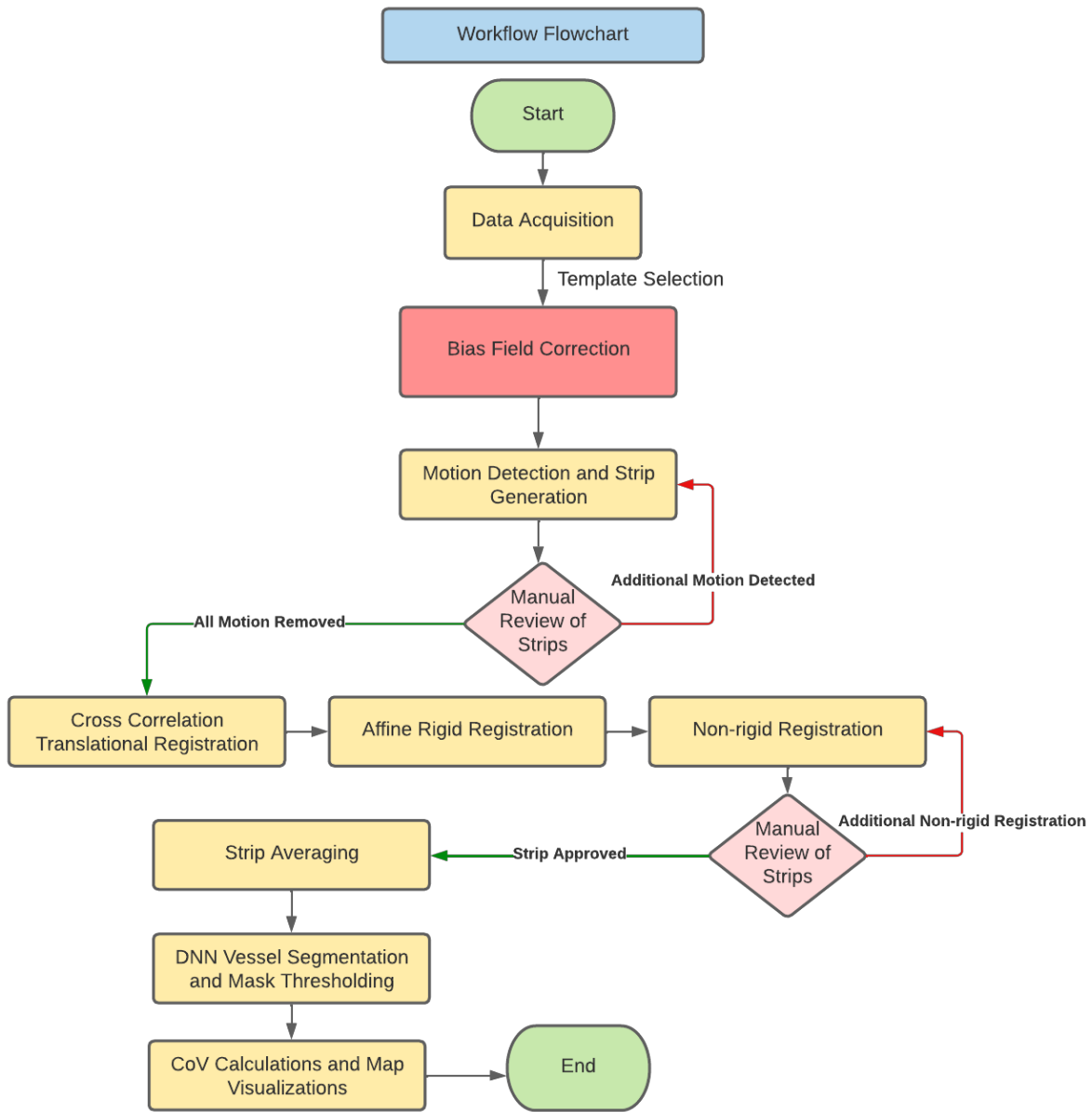


Figure 6: Registration and averaging pipeline flowchart. The red box indicates the new preprocessing step to be included, bias field correction.

2.1 Data Acquisition

Patient imaging sessions were performed at the Eye Care Centre (ECC) of Vancouver General Hospital. This thesis used OCT-A data acquired from the eyes of patients with OAG, NTG, and healthy controls. There were two commercialized machines available for use, the ZEISS PLEX Elite 9000, which utilizes Swept-Source OCT, and the TOPCON Maestro2, which uses Spectral-Domain OCT. Both systems produce images with a high resolution at a high speed [26-28]. The PLEX Elite 9000 was selected for use in research studies as it has a quicker acquisition speed than the Maestro2 and a built-in hardware tracking function which corrects for large saccadic movements [27-28]. The volumetric data acquired has dimensions of 300x1536x300 voxels, resulting in en-face images that are 3x3 mm in size.

2.2 Motion Detection

As it takes several seconds to acquire an OCT-A volume, motion artifacts can occur. Microsaccadic eye movement during imaging can appear as bright stripes, as seen in (A) of Figure 4. Typically, post-processing performed by commercial OCT-A machines removes these bright lines from images [29]. However, some motion artifacts are still present and can be more difficult to detect, as seen in (B) of Figure 4. A combination of automatic motion detection and manual correction is currently in use to identify and remove the motion artifacts.

In the current processing pipeline, the implementation of a cross-correlation algorithm is used to identify motion artifacts in OCT-A images [30]. Briefly, cross-correlation is a measure of the similarity between a vector and a shifted version of a different vector and is commonly used for motion measurement. The cross-correlation of adjacent B-scans is calculated across the OCT-A image, with the maximum peaks and minimum valleys indicating the presence of a motion artifact for removal.

2.3 Registration and Averaging

After image acquisition, all of the serially acquired images need to be registered and averaged. Registration is the process of aligning multiple images in space through a series of spatial transformations [31]. In the existing registration algorithm, the first step is to identify a template image from the batch of acquired images. The template image should be the image with the highest quality and the least number of motion artifacts. Once the template image is selected, all images will be manually reviewed and subdivided into strips if any motion artifacts are present. Figure 7 showcases the subdivision of Figure 4 into individual strips.

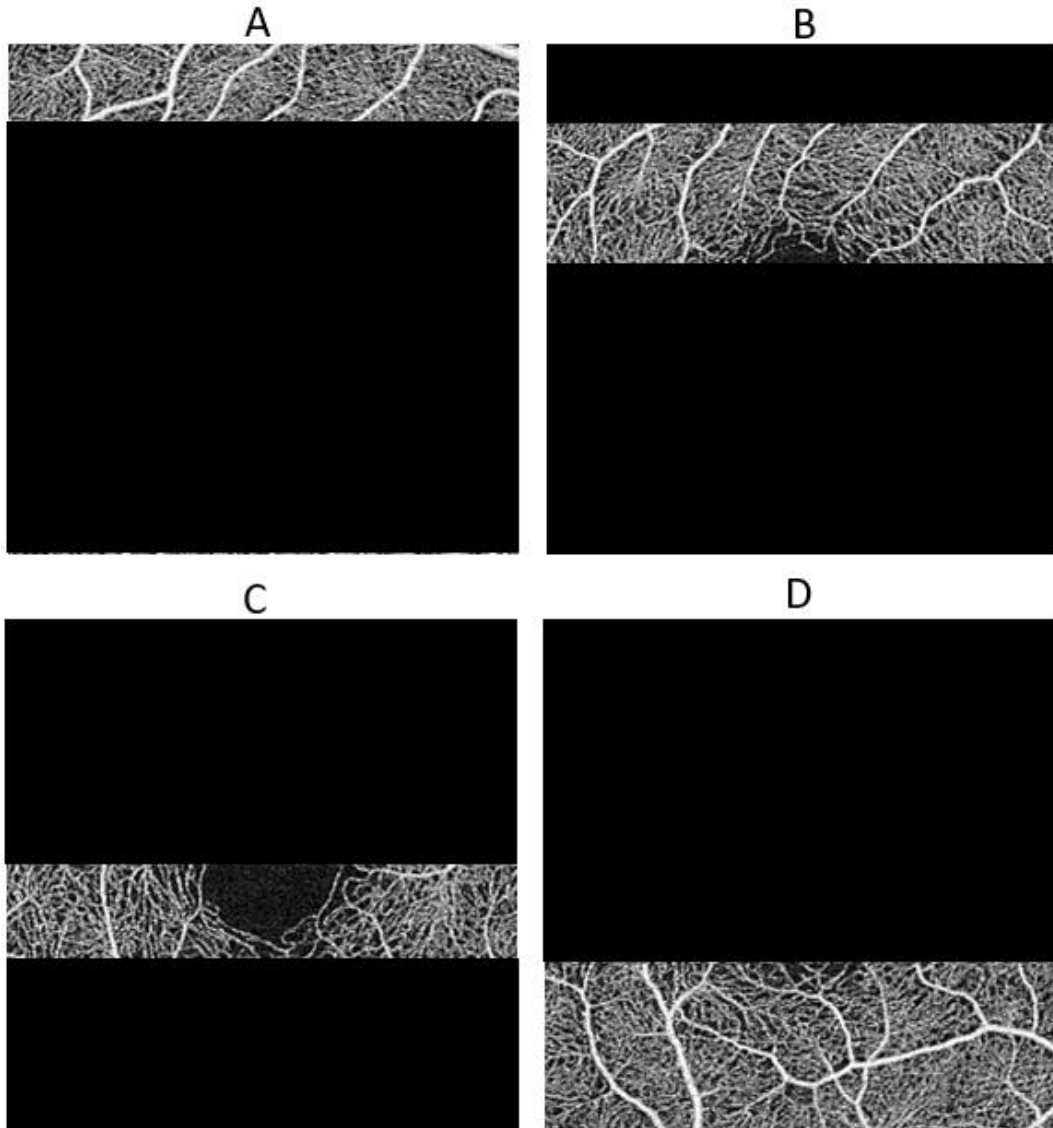


Figure 7: Figure 4 OCT-A subdivided into strips for registration with the removal of motion artifacts.

Once all images have been reviewed and subdivided into strips, they will undergo cross-correlation translational registration, affine rigid registration, and non-rigid registration with the template [16, 17]. Cross-correlation translational registration is used to determine the x and y translation shifts that will result in the position where the strip will best match the template. Next, rigid registration is performed using a combination of the Binary Robust Invariant Scalable Keypoints (BRISK) and Speeded-Up Robust Features (SURF) algorithms. Shared keypoints between the template image and strip identified using both algorithms are considered true and used to estimate an affine transformation function. This type of geometric transformation preserves points, straight lines and planes using translations and rotations. The result of this step is the alignment of the largest blood vessels between the template and strip. Non-rigid registration is then applied to correct for localized vessel mismatch and improve the alignment of finer features. Figure 8 visualizes the result of a strip overlaid with the template before and after

registration. After registration is complete, the final stack of images is averaged together to produce a high-quality OCT-A image, as seen in (B) of Figure 9.

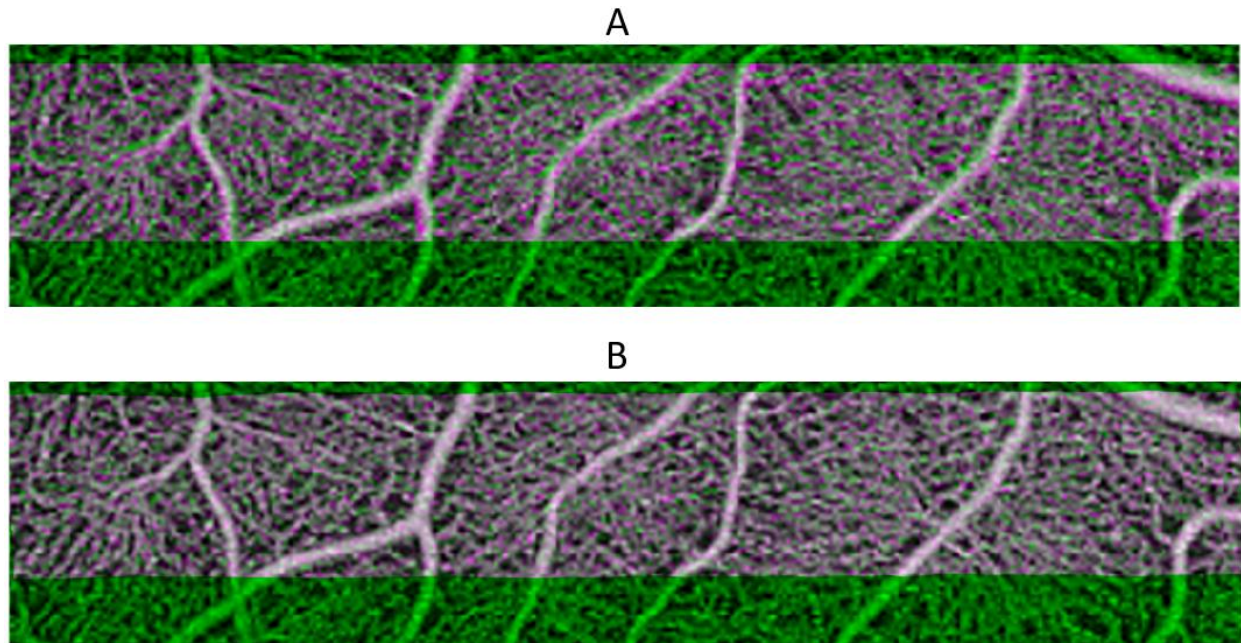


Figure 8: (A) Strip overlaid with the template prior to registration. (B) Strip overlaid with the template after all registration is complete. Green and magenta indicate vessel misalignment while white indicates correct alignment.

2.4 Vessel Segmentation

After registration, the averaged OCT-A image will be given as input into a deep neural network (DNN) to isolate the microvasculature from the background. The DNN used in this algorithm has been shown to outperform other segmentation methods [18]. The output of the DNN, as seen in (C) of Figure 9, will be a probability map with values between 0 and 1, where 1 indicates a high probability of the pixel belonging to a vessel. A mask is then created by thresholding the probability map at a value of 0.5, indicating where the DNN has 50% confidence that each pixel belongs to a blood vessel. The mask is then multiplied to the stack of registered strips to reduce the noise. These noise-reduced strips are then used to calculate the pixel intensity coefficient of variation.

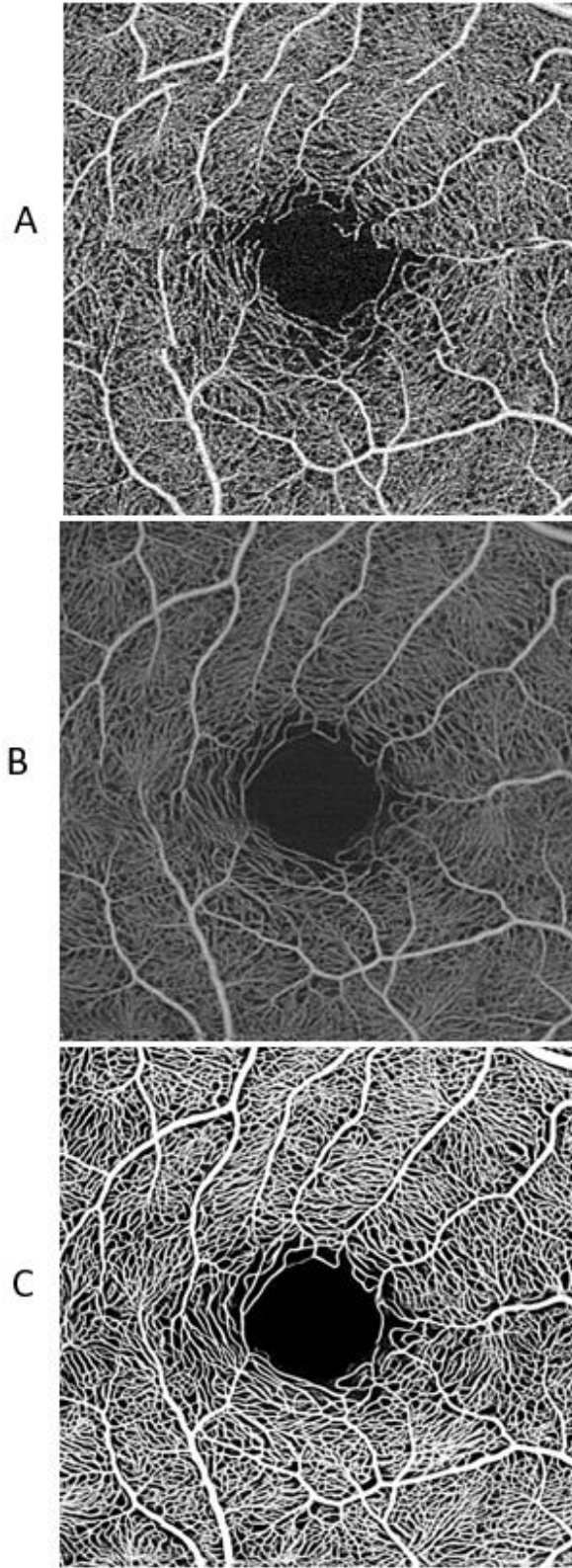


Figure 9: (A) A single OCT-A image with motion artifacts visible. (B) The result of 16 registered images averaged together, producing a high-quality image with clear vessels. (C) The averaged image (B) vessel segmented using a DNN.

2.5 Coefficient of Variation

The methods described in the previous sections are implemented to ensure that acquired OCT-A en-face images are correctly registered and segmented. This registered strip data can then be used to quantify the retinal perfusion heterogeneity through the calculation of the pixel intensity coefficient of variation (CoV). CoV measures the variability of the vascular signal between all of the serially acquired and registered OCT-A images at each pixel location. The input into each CoV calculation is an array with the total number of intensity values at each pixel across all the strip images. The CoV is calculated as:

$$CoV = \frac{std(x)}{mean(x)} \quad (1)$$

A CoV map can be generated that displays the variation in the microvasculature, as seen in (A) of Figure 10. The CoV calculation results are thresholded at 0.5 and linearly scaled between 0 and 1, where 1 represents the highest variation and 0 represents the lowest variation. CoV values in the range from [0 0.3] are considered to have low variation and are typically seen in the large superficial vessels. CoV values in the range from (0.3 0.6) have an intermediate amount of variation while values from [0.6 1] have high variation, typically signifying blinking vessels. Clinical professionals can use the CoV maps and calculations to investigate the differences in retinal perfusion for various diseases [19].

There are some imaging artifacts that can present themselves in CoV maps. Firstly, there can be vertical strips of colour variation in the CoV signal which does not indicate perfusion heterogeneity. These strips are actually artifacts from the strip-based registration processing, and an example is highlighted in (B) of Figure 10. There can also be black regions which is an indicator of a lack of registered strips in an area. CoV measurements are extremely sensitive to artifacts, so it is important to ensure that all processing is done correctly.

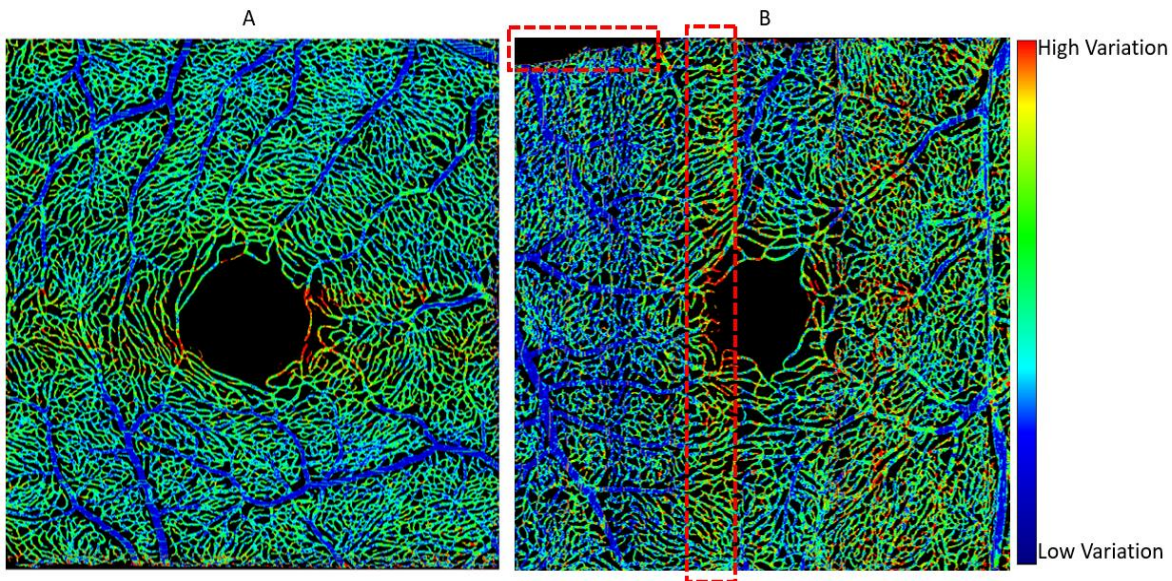


Figure 10: (A) An excellent quality CoV map. (B) A poor quality CoV map with a black region and vertical strip of colour variation highlighted. The color bar indicates the variation from dark blue through to red.

2.6 Summary

In this chapter, the averaging and registration algorithm was introduced, and each component of the pipeline was discussed. The final averaged image can then be used to visualize the retinal perfusion heterogeneity with the use of CoV maps. We may now develop the new preprocessing step in the algorithm, bias field correction.

Chapter 3: Methods for Bias Field Correction

The inclusion of bias field correction in the registration and averaging algorithm described in Chapter 2 will further improve the quality of the OCT-A data for retinal perfusion heterogeneity analysis. This chapter discusses the engineering design specifications for bias field correction and continues with an exploration of each correction approach.

3.1 Bias Field Engineering Design Specifications

Due to the influence of the bias fields present on the OCT-A images, the CoV calculations are affected and will include the presence of the bias artifact. Bias field correction will be the new preprocessing step in the registration and segmentation algorithm towards generating the CoV map. It is hypothesized that successful bias field correction will reduce the variation in the CoV maps, therefore increasing the contrast of regions with actual spatial and temporal flow heterogeneity. There is no universal validation assessment to determine the success of bias field correction. In this thesis, it will be determined through the qualitative and quantitative analysis of the CoV calculations and maps before and after bias field correction. The objective of bias field correction is to change the CoV calculation by 2%.

3.2 Bias Field Design Overview

Many imaging modalities produce the nonuniform intensity illumination due to the imperfect image acquisition process. The consensus for medical images is that the bias field can be thought of as a low frequency artifact and visualized as a smooth intensity varying function across the image [20]. The typical MRI models assume that the image acquired has a bias field that is either multiplicate or additive to it, plus the addition of a noise component. However, for most OCT-A bias field models, there is only a multiplicate component, with an example seen in Equation (2) [21].

$$D'(x, y) = D(x, y) * \frac{Mean(G(S))}{G(S(x,y))} \quad (x = 1, 2, 3, \dots X; y = 1, 2, 3, \dots Y) \quad (2)$$

In Equation (2), $D(x, y)$ is the original en-face angiogram and $D'(x, y)$ is the corrected image. $G(s)$ is the bias field and x and y are the pixel locations of the images of size X and Y .

The bias field may be different in the sequential volumes of a patient, and therefore affects the CoV measurement. The bias field contributes noise to the pixel intensities, and therefore affects the standard deviation and the mean in Equation (1). This can cause artifactual changes in the CoV maps that do not indicate the perfusion in the microvasculature.

There are two classifications for the approaches that are used for correcting the bias field artifact, prospective or retrospective methods [20, 25]. Prospective correction methods attempt to reduce the bias field by minimizing the inaccuracies during the image acquisition process. Retrospective correction methods aim to reduce the bias field using the characteristics of the medical images and typically involve a two-step process. The first step is estimation of the bias field, and the

second step is a division, multiplication or addition to remove the bias field [20-25]. Bias field correction will result in enhanced OCT-A images and an increased accuracy for the perfusion heterogeneity analysis. The following subsections of this chapter describe the initial bias field design attempts, the problems encountered with each approach and revisions performed to reach the final design.

3.3 Bias Field Correction Using the En-Face OCT-A Images Produced by the Zeiss Plex Elite 9000

The first method of bias field correction utilizes the two-dimensional (2-D) en-face OCT-A images directly downloaded from the Zeiss Plex Elite 9000. The images have a pixel dimension of 1024x1024, so there is post-processing performed by the device which increases the size of the image compared to the original volume data. Equation (3) showcases the 2-D Gaussian filter [32]. The variables x and y represent the distances from the horizontal and vertical axes respectively, while σ is the standard deviation of the Gaussian function.

$$g(x, y) = \frac{1}{2\pi\sigma^2} e^{-(x^2+y^2)/(2\sigma^2)} \quad (3)$$

This type of filter is a convolution operation that is typically used to remove noise and detail from an image with a blurring effect. In the first method of bias correction, an illumination bias field was produced by applying a Gaussian filter with a pixel standard deviation that was 10% of the image size in pixels. Figure 11 showcases the results of bias field correction with the gaussian filter using Equation (1).

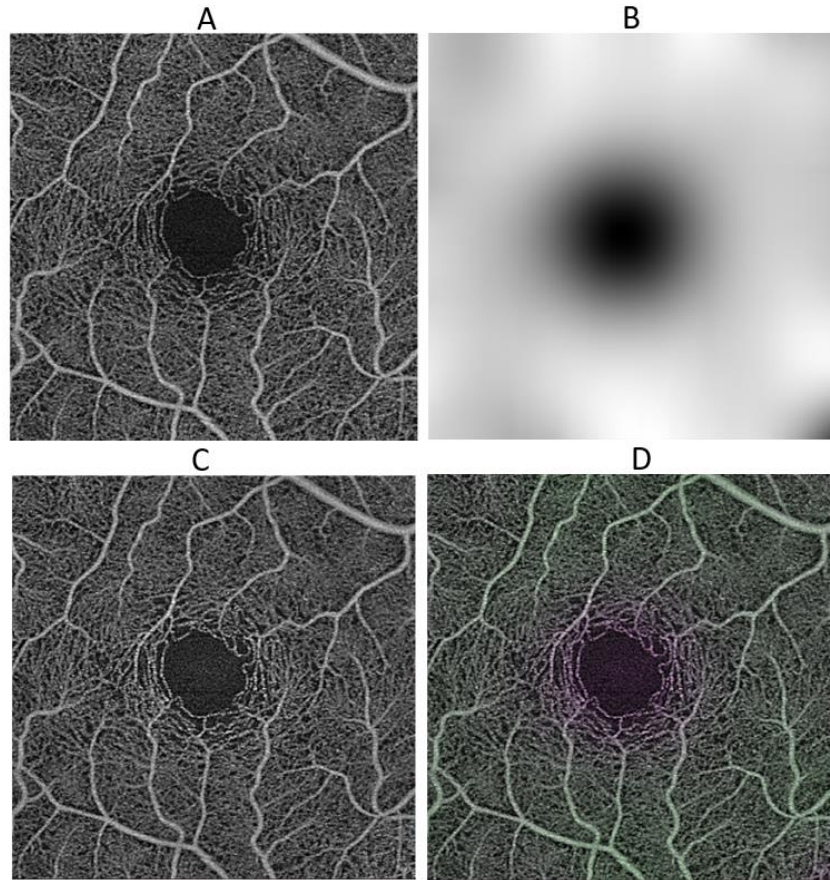


Figure 11: Bias field correction using OCT-A images. (A) Original OCT-A 3x3 mm image acquired from the ZEISS PLEX Elite 9000. (B) Bias field artifact of (A) seen with a Gaussian filter [21]. (C) Corrected OCT-A image with the bias field removed. (D) Overlay of (A) and (C) visualizing the intensity differences after the bias field is removed.

Using this approach, we can see that the bias field is heavily influenced by the FAZ, as seen in (B) of Figure 11. This type of bias correction increases the intensities of the vessel regions in the FAZ relative to the intensities everywhere else, as seen in the intensity overlay plot shown in (D) of Figure 11. The drawback with only using OCT-A images is that they are susceptible to variation in intensity and artifacts can appear due to various ocular conditions as well as defocus. Shadows and signal loss due to floaters, cataracts and other media opacities can appear on the images and are not representative of perfusion loss in vessels [33-34].

3.4 Bias Field Correction Using En-Face Images Produced from the Raw OCT-A Volume Data

The previous section discussed a bias field correction method using the 2-D en-face images produced by the Zeiss Plex Elite 9000. The preliminary results demonstrated the issue and showed proof of concept results. However, further improvements can be achieved by iterating on the algorithm. Firstly, it is unknown what processing is performed on the volume by the proprietary algorithms of the Zeiss device to extract and visualize the images. Additionally, there is no

noticeable intensity variation across the 2-D Zeiss produced images when visually examining them. This section will discuss a method to correct for the bias directly from the OCT-A volumetric data.

Using the OCT volume which contains anatomical structural data, bias fields will be estimated that represent the intensity changes due to the tilt of the retina. The tilt is related to the focal position, and hence is a systematic cause of bias that needs to be corrected. Two bias fields will be created, one in the fast scan direction and the other in the slow scan direction. These bias maps will then be applied to the en-face images produced from the OCT-A vasculature data to remove the bias field artifact. Figure 12 provides a visualization of the mean en-face projection of the entire OCT volume as well as a B-scan in the fast scanning and slow scanning directions. The axial mean of the pixel intensities in the fast-scan B-scan represents a column in the mean en-face projection, signified with the red line in (C) of Figure 12. The axial mean of the pixel intensities in the slow-scan B-scan represents a row in the mean en-face projection, represented by the green line in (C) of Figure 12.

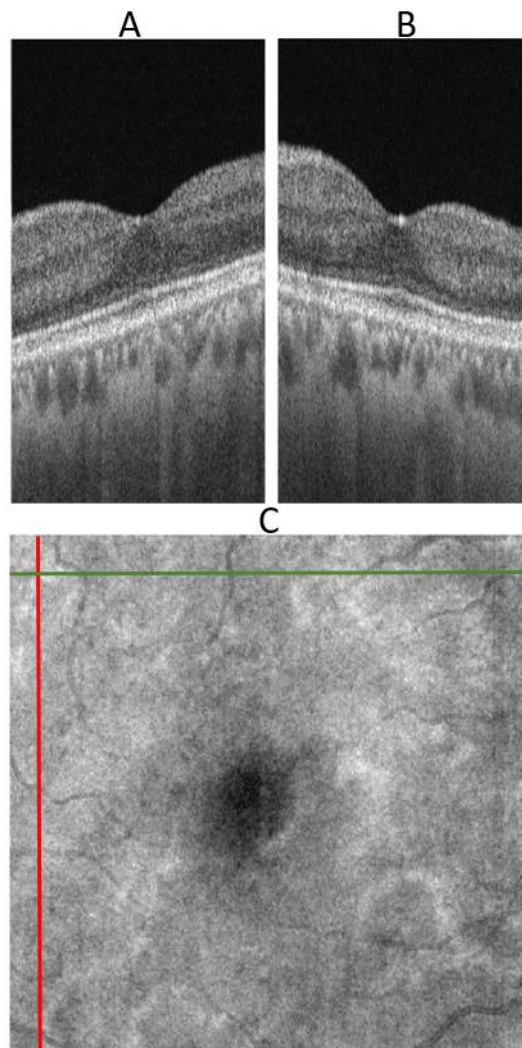


Figure 12: (A) Fast-scan B-scan of the OCT volume. (B) Slow-scan B-scan of the OCT volume. (C) Mean en-face projection of the OCT volume.

The initial attempt at generating the mean en-face OCT-A projection used the entire A-scan depth when calculating the axial mean value at each location. However, this deteriorated the signal quality by including measurements of noise as well as the bright back-scattered signal from the choroid, so segmentation of retinal layers was required. To generate the en-face OCT-A images from the raw OCT-A data, the following processing steps are performed. Three-dimensional bounded variance smoothing is applied to the OCT volume to enhance the boundaries between retinal layers and reduce the effect of speckle. The retinal layers of the smoothed OCT volume are then segmented using a MATLAB 3-D graph-cut algorithm [35, 36]. Figure 13 showcases the difference in an OCT B-scan before and after smoothing, while Figure 14 provides a B-scan with the retinal layers identified [37]. The internal limiting membrane (ILM), the external limiting membrane, the photoreceptor layer boundary and Bruch's membrane are the layers of interest segmented. The ILM to ELM region identified on the OCT volume is used to generate the en-face OCT-A image from the raw OCT-A volume data. The region between the ELM and Bruch's membrane will allow for the estimation of the bias field. The ELM-BM region contains the photoreceptor cells, light sensitive cells with a strong contrast visible on an OCT B-scan.

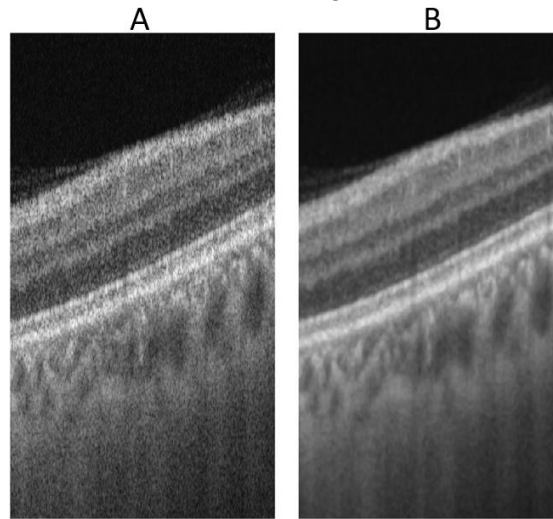


Figure 13: OCT B-scan before (A) and after (B) 3-D bounded variance smoothing.

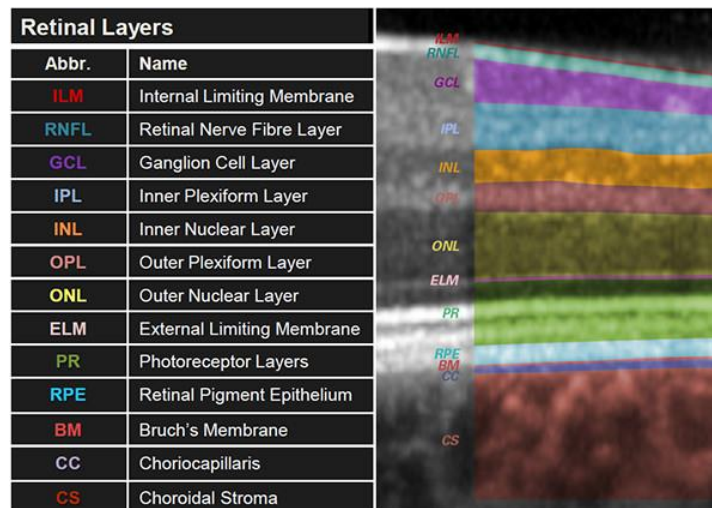


Figure 14: Retinal layer subdivisions on an OCT B-scan.

After segmentation is performed, the region between the ELM and Bruch's membrane will allow for the estimation of a bias field. For the fast-scan and slow-scan B-scans, the average pixel intensities between the PR-BM region for each A-scan will be calculated. This process is repeated across all of the B-scans in the volume in both scanning axes, resulting in two 300x300 averaged matrices. The matrices are then averaged to create two 1x300 vectors, representing the intensity tilt across the retina for both the fast-scan and slow-scan directions. Using the method of least squares, polynomial regression curve fitting is then applied to fit the average intensity plot to a polynomial function. The polynomial function approximation is of the form

$$\sum_{j=0}^M w_j x^j \quad (1)$$

where M is the order of the polynomial, x^j denotes x raised to the power of j and w is the polynomial coefficient. Initially, a higher degree polynomial was estimated to best fit the data. However, after testing with varying degrees, a polynomial of degree 1 was selected to exclude intensity variations due to shadows and other artifacts that reduce the intensity over a range of A-scans throughout multiple B-scans. Figure 15 showcases an example of shadows which project into the region used for bias field estimation.

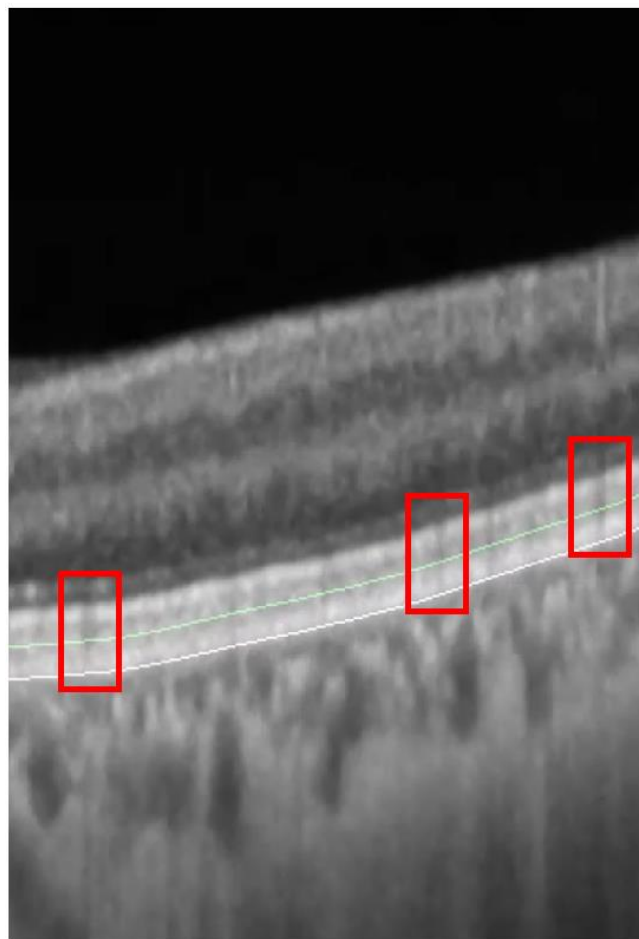


Figure 15: Shadow regions shown in the red boxes can decrease the intensity of the A-scan position, so a linear polynomial approximation was selected to minimize this affect.

The method described in this section aims to correct for the bias produced by the intensity tilt of the retina. However, using the individual segmentations of the retinal layers will result in an inaccurate en-face image and can decrease the accuracy of the bias field estimations. This issue would be caused by a different number of A-scan pixels between the segmentation boundaries and would not represent the bias that this approach would be correcting. The en-face image would have averaging related shadows artifacts and the bias estimation would have a fluctuating plot. The solution chosen for this problem was to accurately segment the BM boundary and then vertically shift the segmentation upwards, ensuring the shift is the same throughout all B-scans. Figure 16 showcases the region used for bias field estimation while Figure 17 visualizes the en-face angiogram produced from the raw volume data between the shifted BM boundaries. Figure 18 provides the average intensity plot in blue and the polynomial approximation in red for both the fast-scan and slow-scan directions.

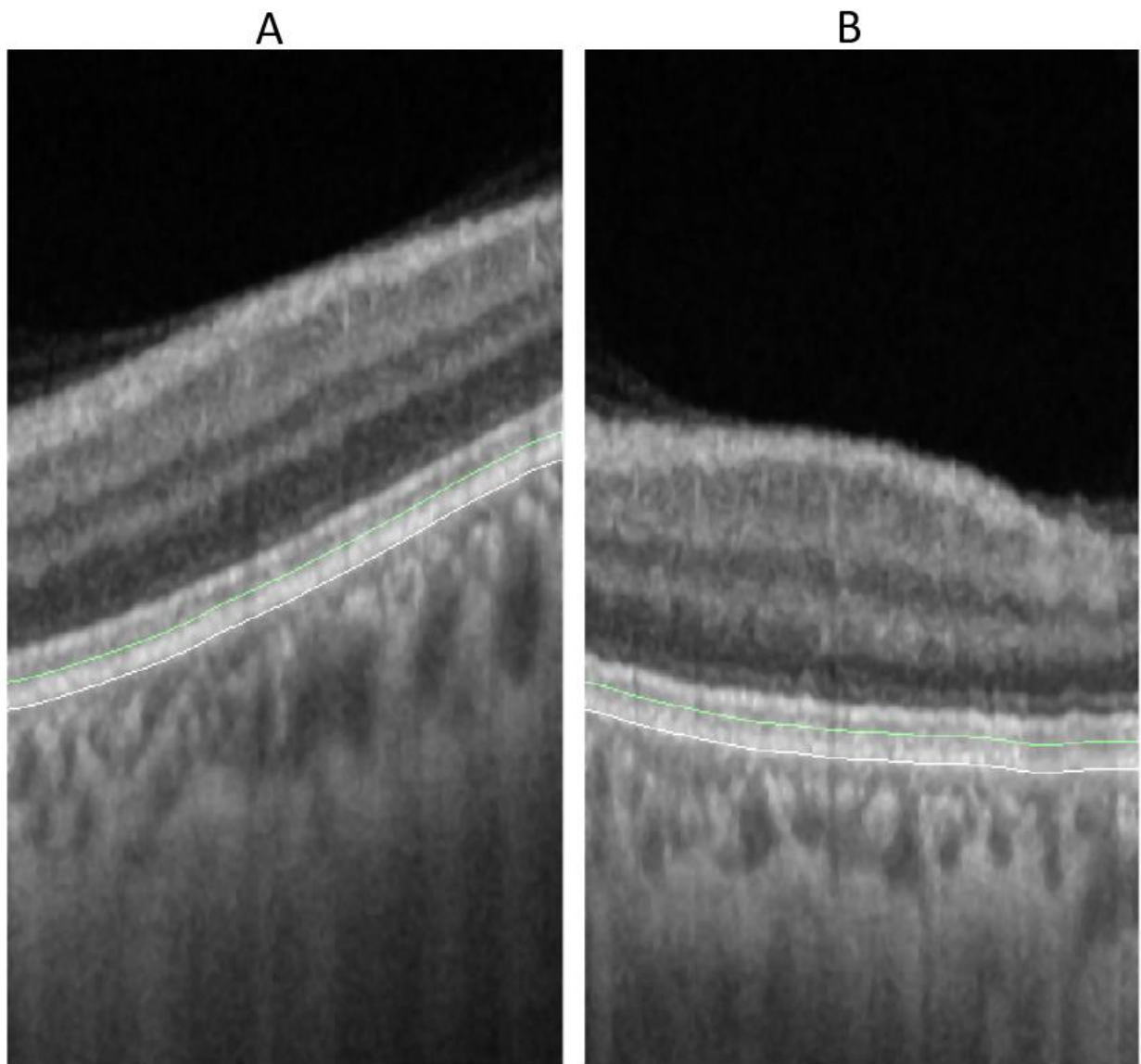


Figure 16: (A) Fast-scan view and (B) slow-scan view showing the BM and shifted BM segmentation boundaries.

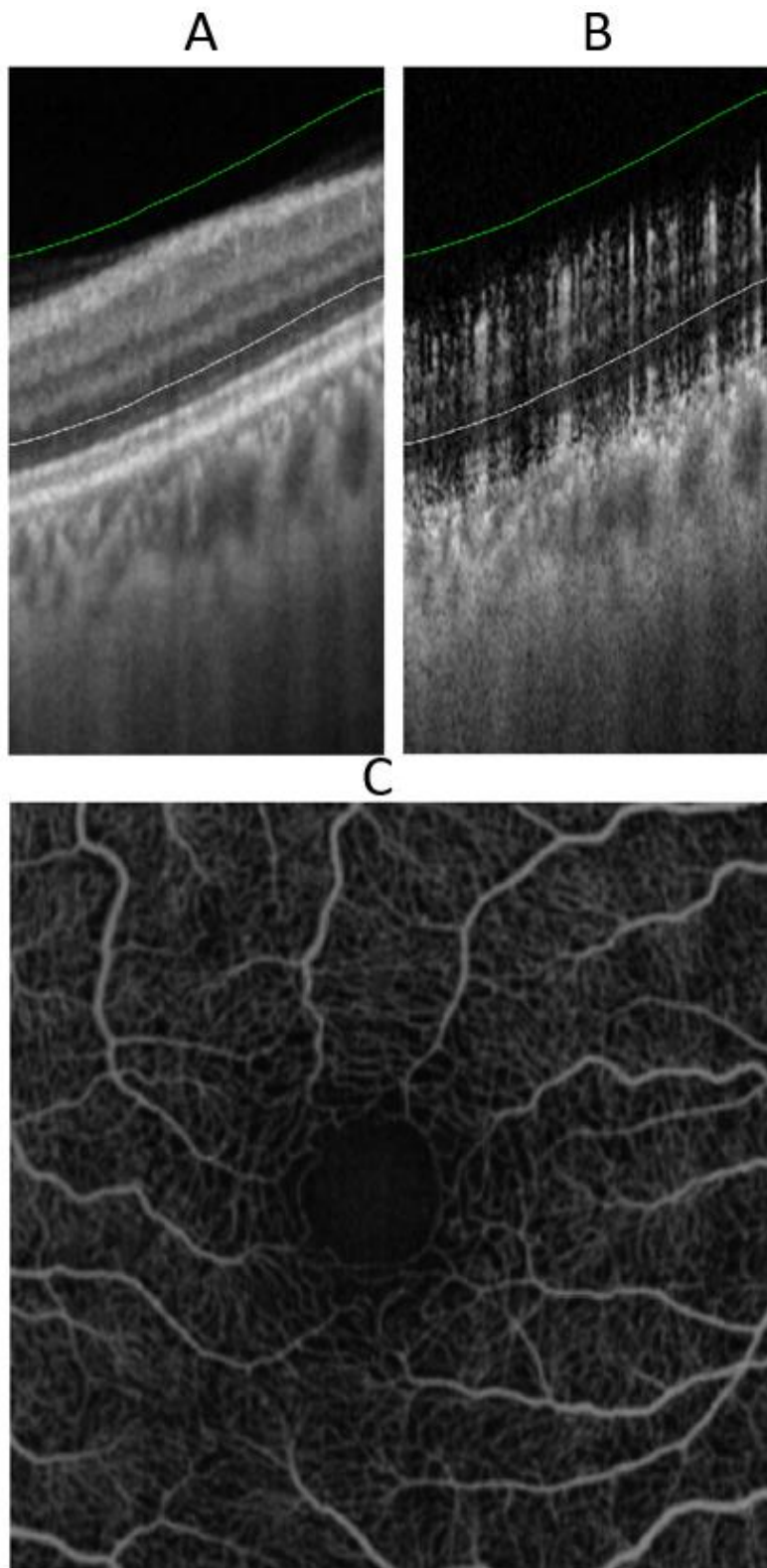


Figure 17: Shifted segmentation of the BM overlaid on (A) an OCT B-scan and (B) an OCT-A B-scan. (C) OCT-A en-face image produced from the averaged intensity values in the axial direction between the layers shown in (B).

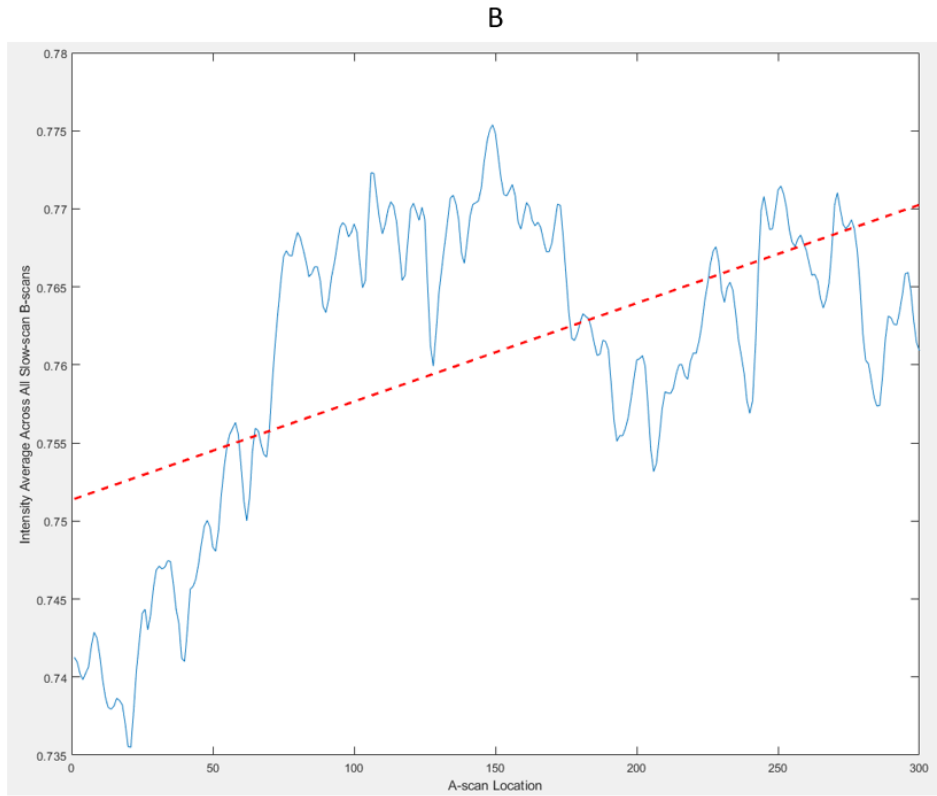
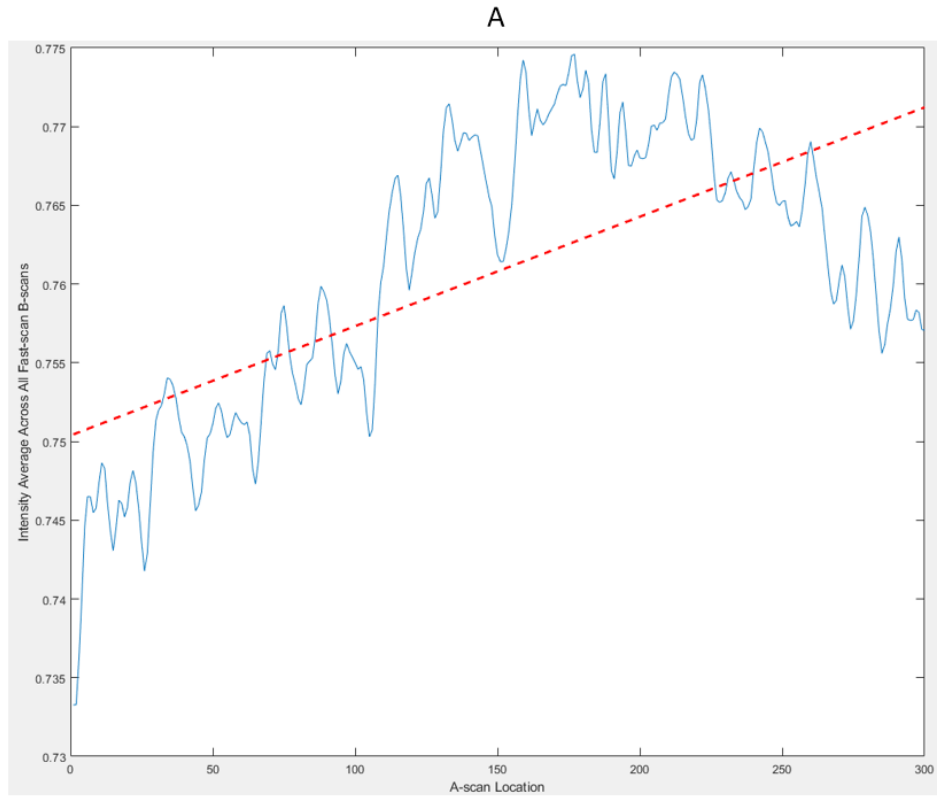


Figure 18: (A) Fast-scan averaged intensity plot and linear polynomial approximation. (B) Slow-scan averaged intensity plot and linear polynomial approximation.

The polynomial approximation is repeated across a matrix to produce the bias fields seen in Figure 19. Before correcting the original image, the fast scan bias field must be rotated 90° to ensure that it is applied to the correct axis. The bias fields are then applied to the en-face image using Equation (2). The uncorrected and bias corrected OCT-A images are then normalized, with an example seen in Figure 20 below.

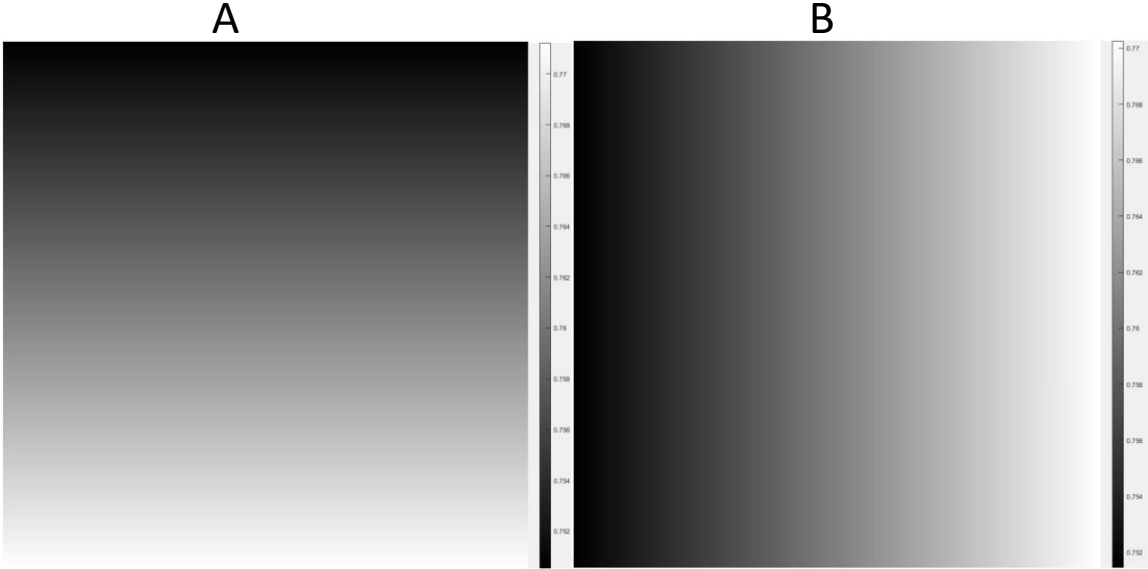


Figure 19: (A) Rotated fast-scan and (B) slow scan bias field estimations from the polynomial approximations in Figure 18.

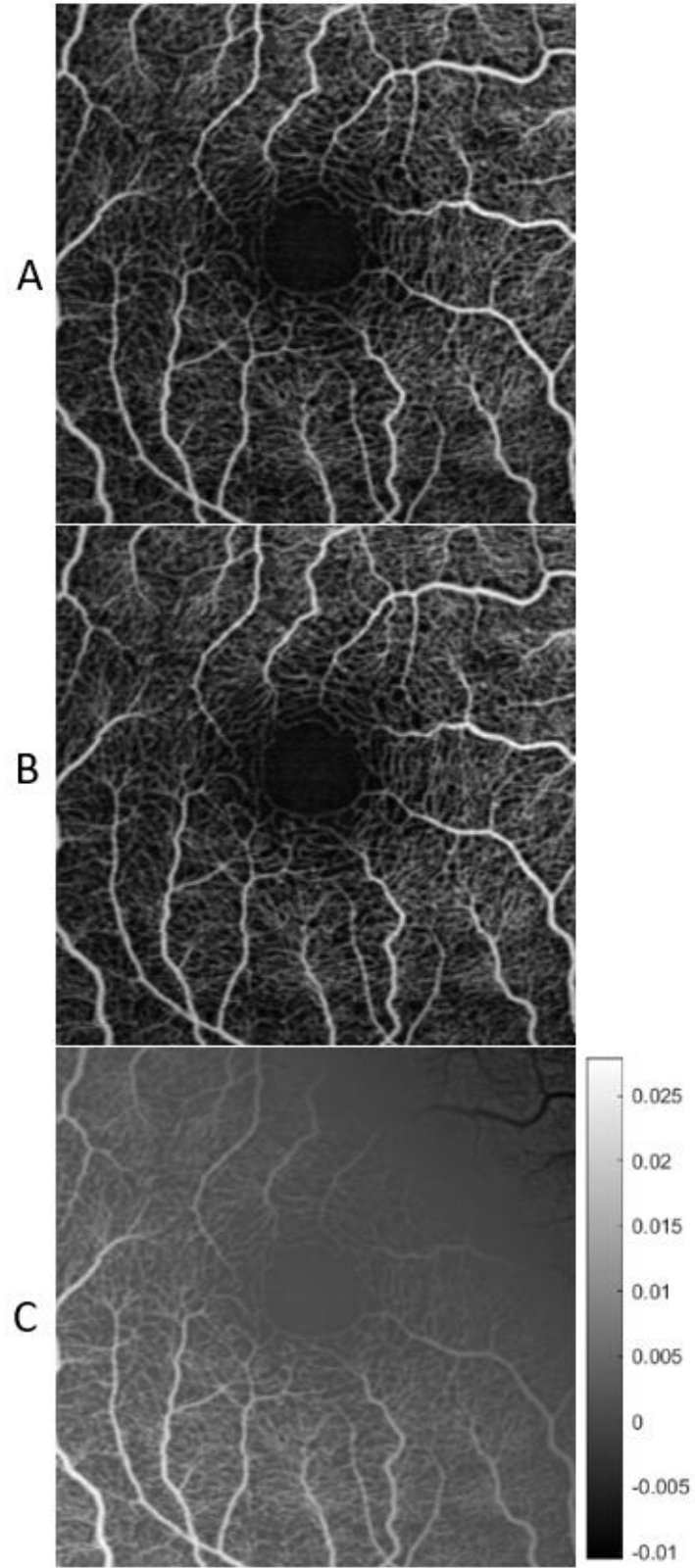


Figure 20: A rotated single en-face image normalized (A) before bias correction and (B) after bias correction using Equation (2). (C) Intensity difference of (A)-(B).

The 2-D OCT-A images produced by the Zeiss Plex Elite 9000 images will be processed through the registration and averaging pipeline. The registration transformations that occur on these images will also be applied to the normalized en-face images produced from the raw OCT-A volume data. Before this can happen, the en-face images need to be rotated 90 degrees and resized to 1024x1024 from the current 300x300 pixel dimensions. Resizing the images will use the method of bilinear interpolation, where the value to be calculated is a weighted average of the of pixels in the nearest 2-by-2 neighborhood.

There are three approaches to visualize the CoV maps for the en-face images produced from the OCT-A volume. The first option involves using the DNN to segment the averaged images directly. However, as the DNN was created using the 2-D Zeiss images, the results of the network on the volume produced images is quite poor. Figure 21 displays the DNN output on the 2-D Zeiss and volume produced en-face OCT-A images. The second approach is to display the CoV maps without the background noise component removed. In Figure 22, a CoV map with the background included is shown, but it would be difficult to make any meaningful conclusions of the retinal perfusion from this map. The third method involves using the DNN output and mask produced for the 2-D Zeiss averaged image and multiplying it to the averaged en-face image created from the volume. Before this can occur, the 2-D Zeiss averaged image and the volume-produced averaged image must be overlaid to ensure that there is good pixel to pixel correspondence, as seen in Figure 23. After verification, the mask can be multiplied to the image and the CoV calculated. This is the method that was used for the remainder of the processing and the results as described in the next chapter.

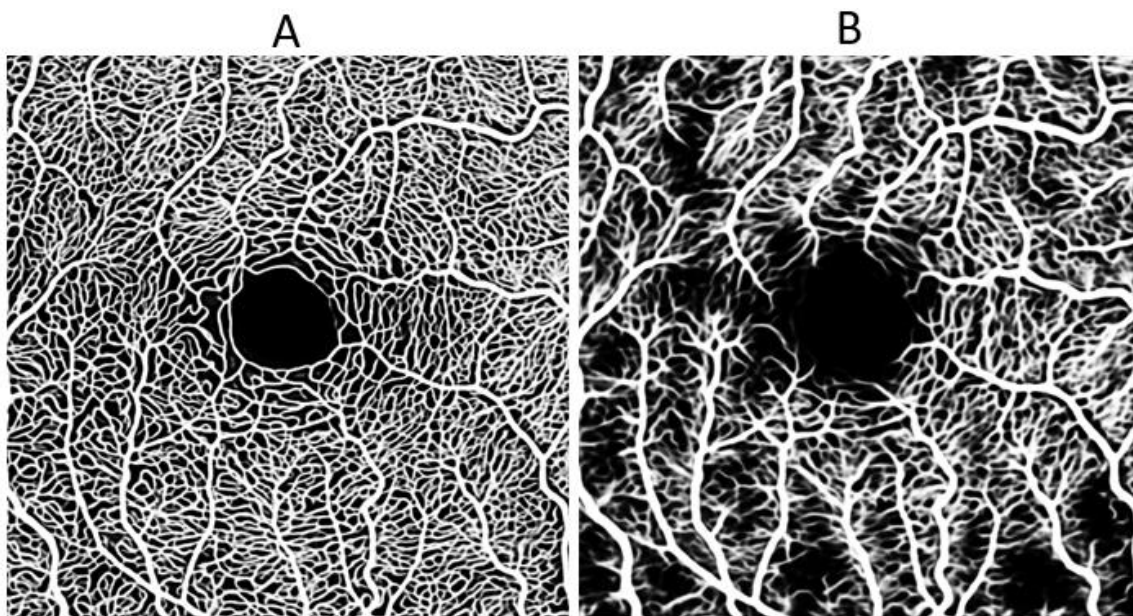


Figure 21: Comparison between the result of the DNN for vessel segmentation on (A) the 2-D OCT-A image from the Zeiss device and (B) the OCT-A image produced from the volume.

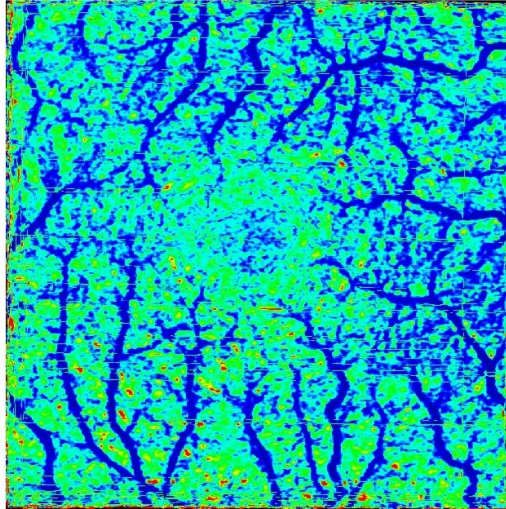


Figure 22: CoV map with the inclusion of the background component.

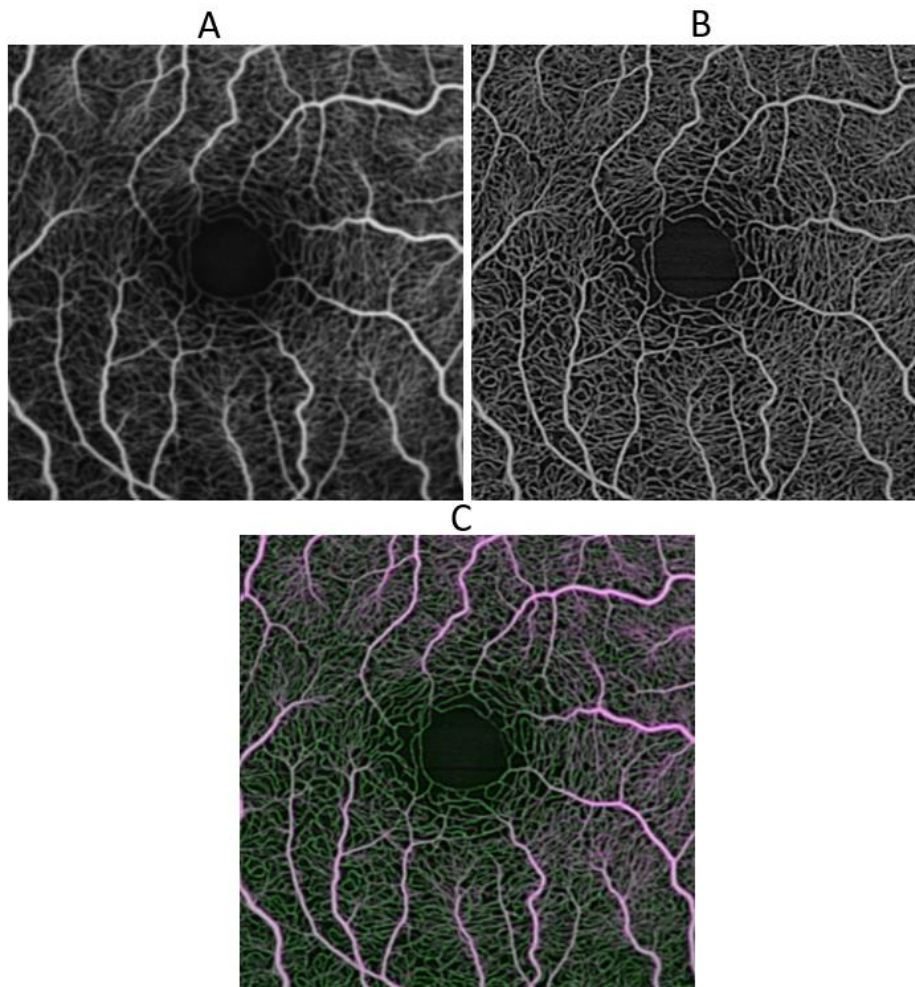


Figure 23: Averaged en-face OCT-A image from (A) the 3-D volume data and (B) the 2-D Zeiss data. (C) The overlay between (A) and (B) ensuring pixel to pixel correspondence.

3.5 Changes to CoV Map Visualization

In the current algorithm, the CoV values are thresholded at 0.5 and scaled between 0 and 1 for display using CoV maps. However, because this is performed individually for each dataset, the colour classification range of the CoV values shown is not accurate when comparing the maps for subjects with different diseases. Instead, we should determine the maximum CoV value across all of the datasets in the study and then set the value as the maximum colour in the display range. This should amplify the changes seen in the microvasculature when comparing the maps between different subjects in the study. One issue with this approach is that if there are any registration artifacts, which can occur particularly around the edges of the averaged image due to a minimal number of strips, they can skew the maximum range with a high CoV value. A solution to this is to limit the CoV values used to find the maximum range to the FAZ region across all datasets, with an example seen in Figure 24. One downside to this approach is that if we have a blinking vessel outside of the FAZ, it would not be included when deciding the maximum CoV value.

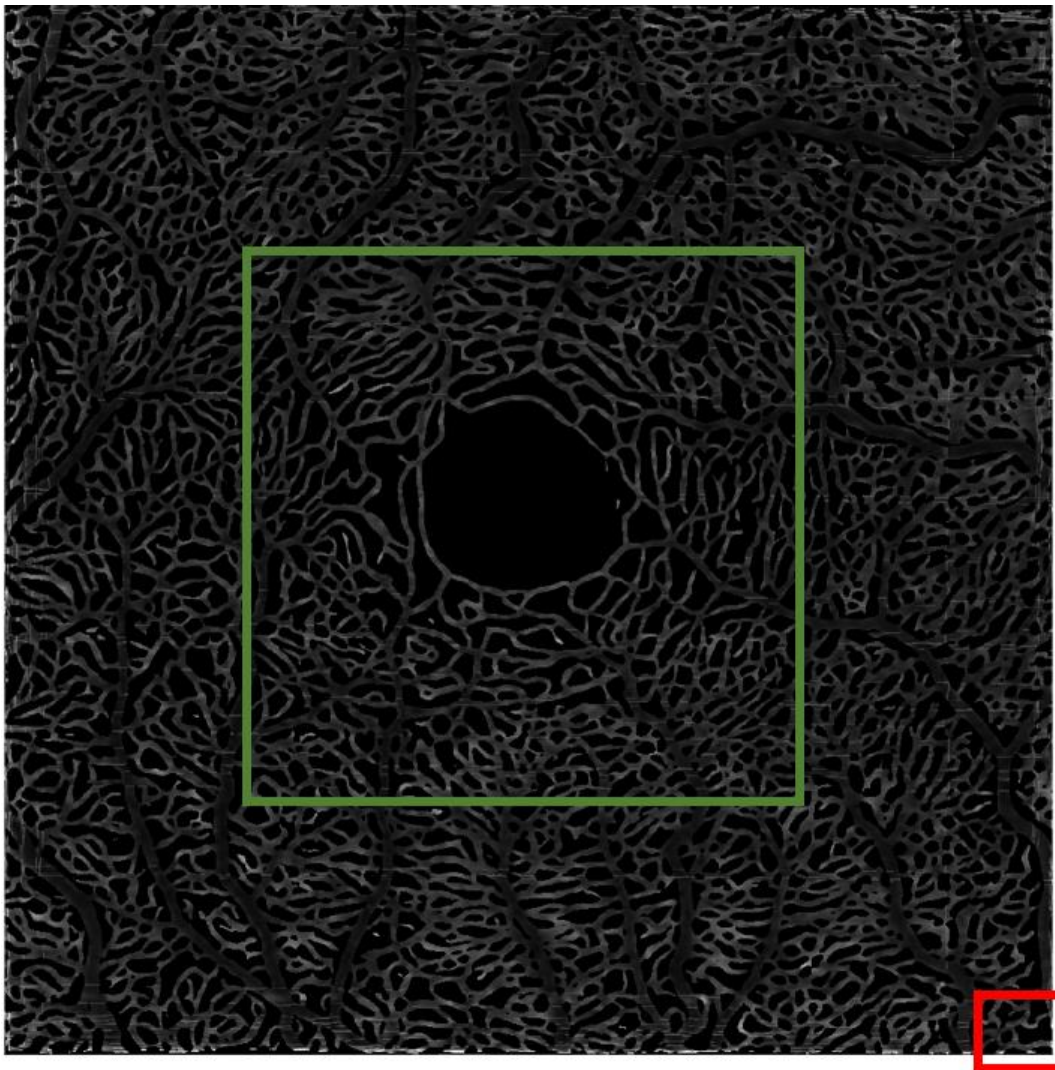


Figure 24: Grayscale visualization of the CoV values. The red box contains the maximum CoV value, while the green box indicates the suggested region to select the maximum CoV value from.

3.6 Bias Field Correction Pipeline Flowchart

Figure 25 below provides an overview of the bias field correction pipeline described in this chapter.

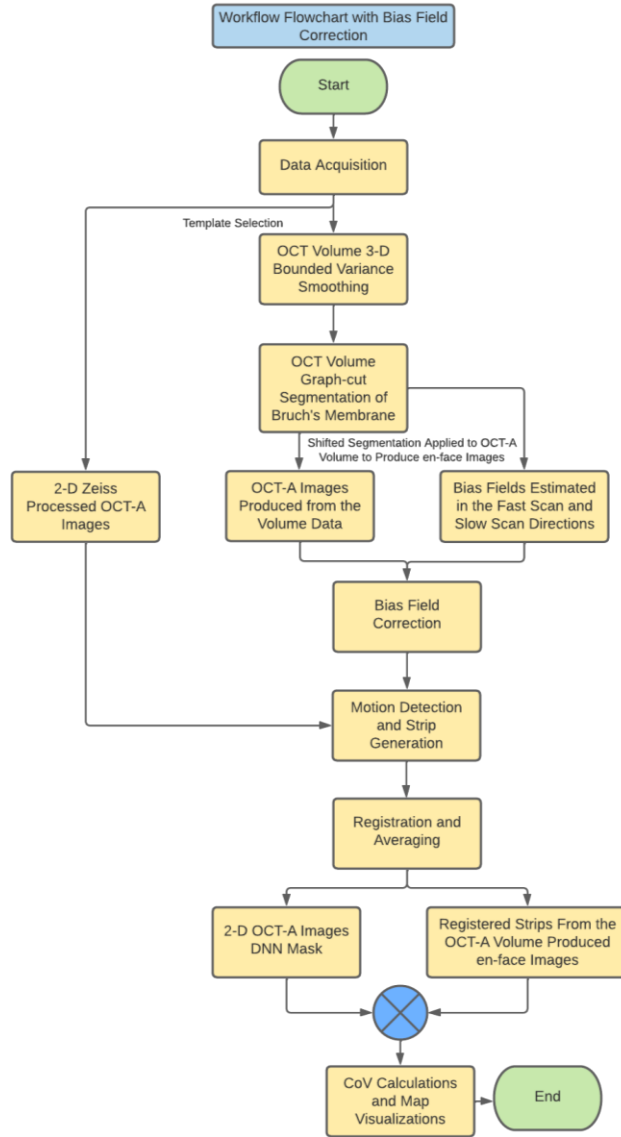


Figure 25: Bias field correction pipeline flowchart.

3.7 Summary

This chapter discussed the need for bias field correction as the new preprocessing operation in the registration and averaging algorithm. The final method of bias field correction was achieved after an iterative design process, and another approach for visualizing the CoV maps was introduced. We may now review the results of this work in the next chapter.

Chapter 4: Results

This chapter examines the impact of the developed bias field correction method on the 3x3 mm en-face OCT-A images produced from the raw volumetric data. This chapter will visually compare and quantify the differences in the uncorrected and bias corrected averaged OCT-A images and CoV maps.

4.1 Visual Comparison of Uncorrected vs. Bias-Corrected OCT-A Images

To correct for the brightness inhomogeneity produced by the tilt of the retina, the method in the previous chapter was employed. The averaged OCT-A images produced from the volume are created using the same registration transformations applied to the 2-D Zeiss processed images. For each dataset, an averaged image and CoV map were produced for the uncorrected and bias corrected en-face OCT-A images produced from the raw volume data.

The processed images of three subjects are shown in this chapter. Column (A) of Figure 26 shows little observable intensity changes across a single image after bias correction, however, the averaged images in column (B) showcase a greater change. This is the expected result as multiple bias corrected volumes have been registered and averaged together. Figure 27 and Figure 31 provide a comparative visual assessment of the uncorrected and bias field corrected CoV maps for Subject 1 and Subject 3, respectively. The highlighted sections in these figures show an increase in the variability of the microvasculature, with less dark blue being visible after bias correction. The opposite affect can be seen in Figure 29 for Subject 2, with more blue becoming prominent after bias field correction.

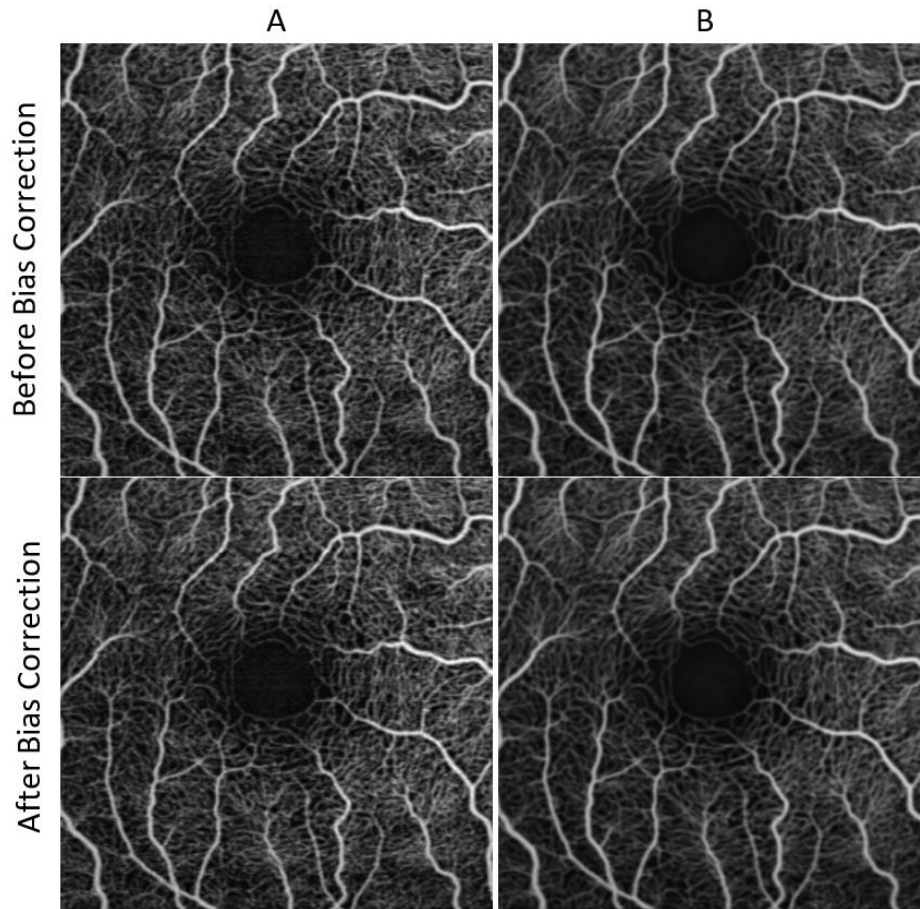


Figure 26: Column (A) showcases a single image before and after bias correction for Subject 1 OD, a male with NTG. Column (B) showcases the averaged images before and after bias correction.

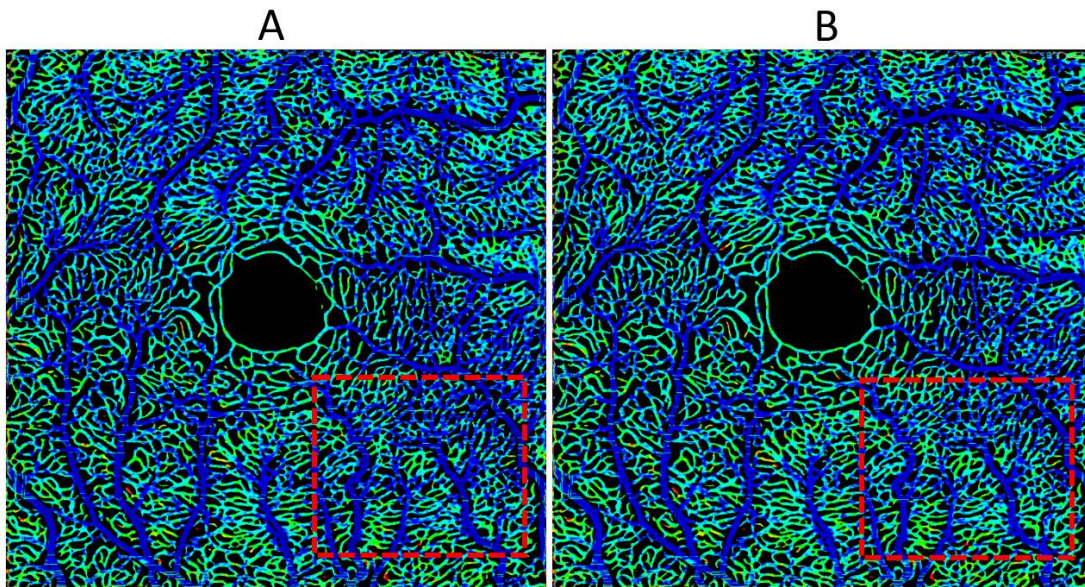


Figure 27: CoV maps for Subject 1 (A) before bias correction and (B) after bias correction.

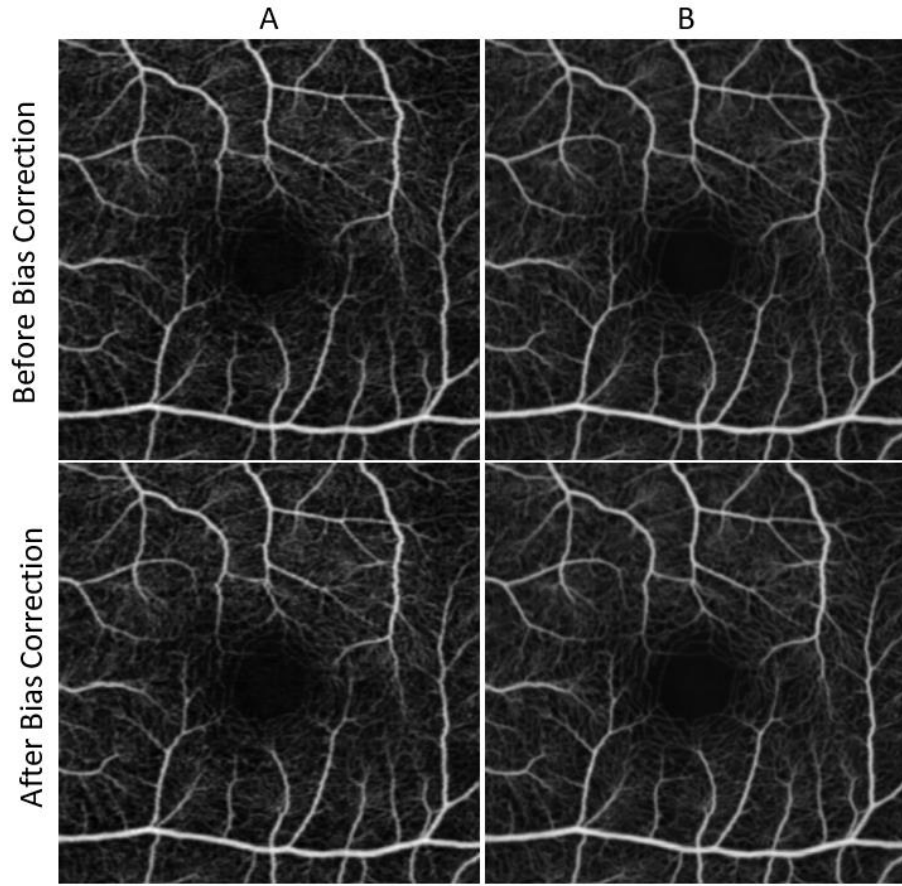


Figure 28: Column (A) showcases a single image before and after bias correction for Subject 2 OS, a male with POAG. Column (B) showcases the averaged images before and after bias correction.

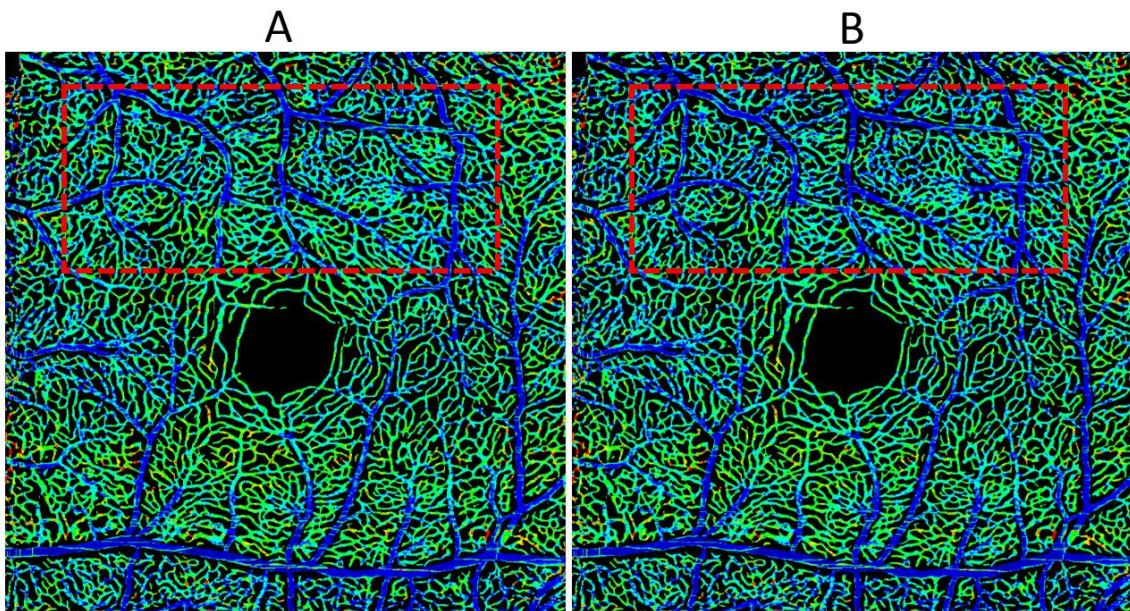


Figure 29: CoV maps for Subject 2 (A) before bias correction and (B) after bias correction

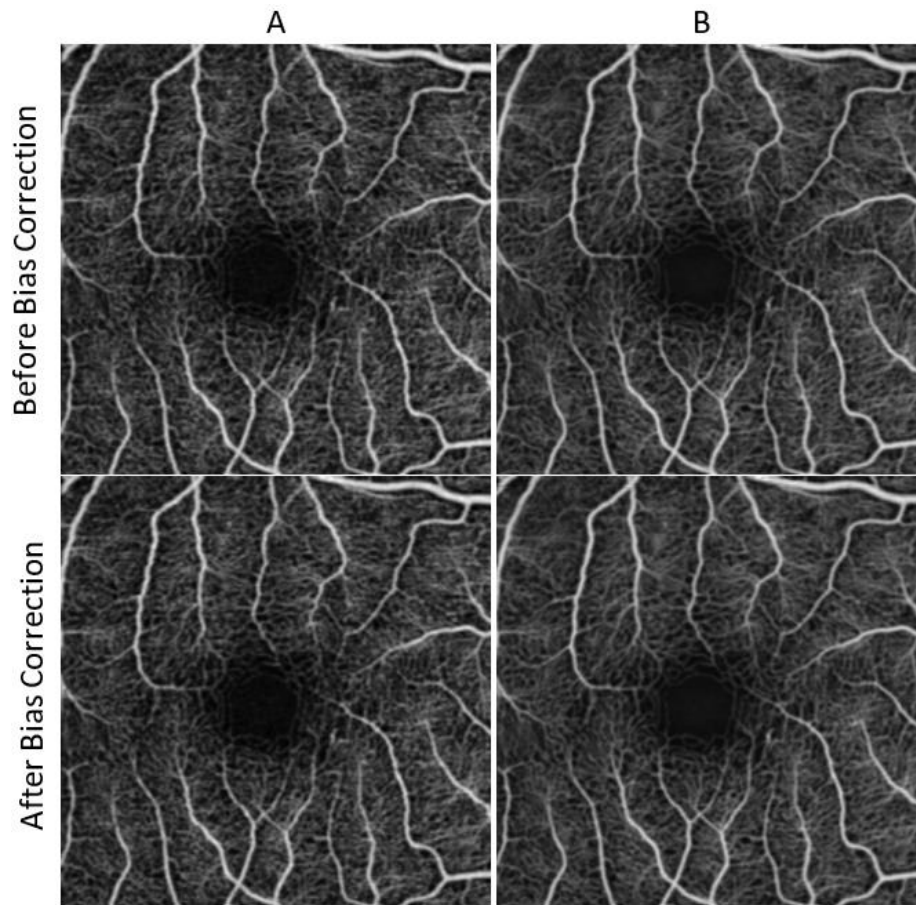


Figure 30: Column (A) showcases a single image before and after bias correction for Subject 3 OD, a healthy male. Column (B) showcases the averaged images before and after bias correction.

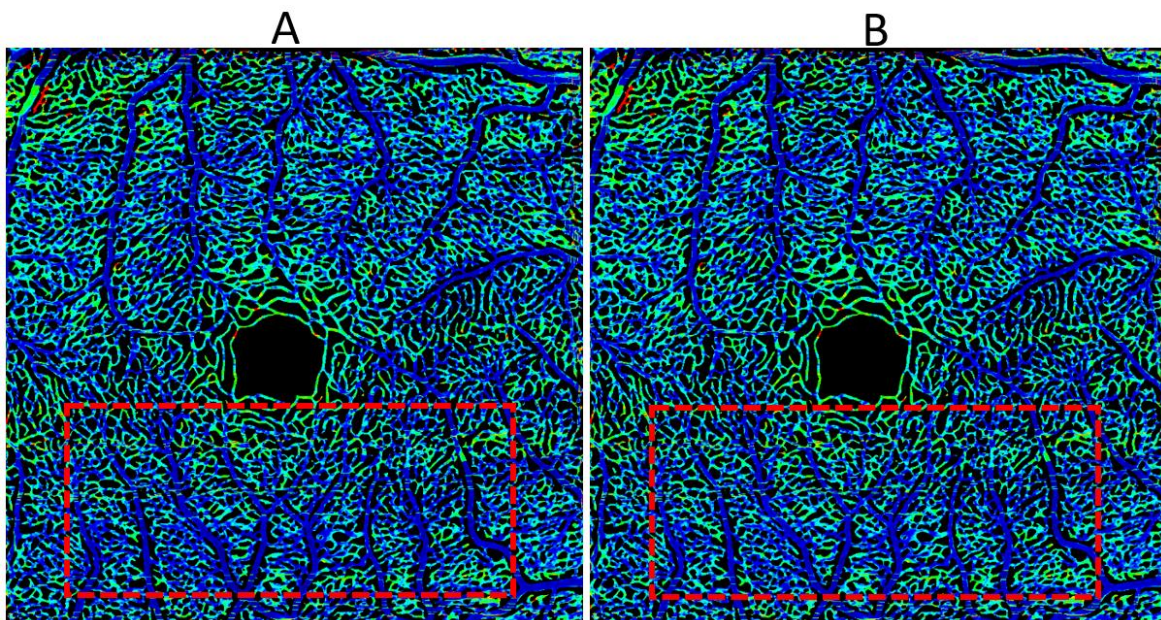


Figure 31: CoV maps for Subject 3 (A) before bias correction and (B) after bias correction

4.2 Quantitative Comparison of Uncorrected vs. Bias-Corrected OCT-A Images

Table 1 provides the CoV calculations for the three subjects before and bias correction. The results seen in the previous section qualitatively can also be interpreted from the CoV calculations. For Subject 1, an increase in the whole image CoV value from 0.1762 to 0.1802 represents a decrease in the blue coded vessels. The whole image CoV for subject 2 has decreased after bias correction, while Subject 3 has increased. The CoV calculations are also determined for each quadrant and a 1.5mm square centered around the FAZ, as seen in Figure 32.

Subject	Bias Correction	Quadrant 1	Quadrant 2	Quadrant 3	Quadrant 4	Whole Image	1.5mm FAZ
Subject 1 Male OD, NTG	Uncorrected	0.1767	0.1677	0.1900	0.1714	0.1762	0.1857
	Corrected	0.1773	0.1670	0.1954	0.1821	0.1802	0.1892
Subject 2 Male OS, POAG	Uncorrected	0.2221	0.2226	0.2324	0.2210	0.2245	0.2410
	Corrected	0.2083	0.2146	0.2304	0.2162	0.2173	0.2334
Subject 3 Male OD, Control	Uncorrected	0.1798	0.1708	0.1674	0.1639	0.1706	0.1806
	Corrected	0.1807	0.1701	0.1708	0.1666	0.1721	0.1827

Table 1: CoV calculations before and after bias correction.

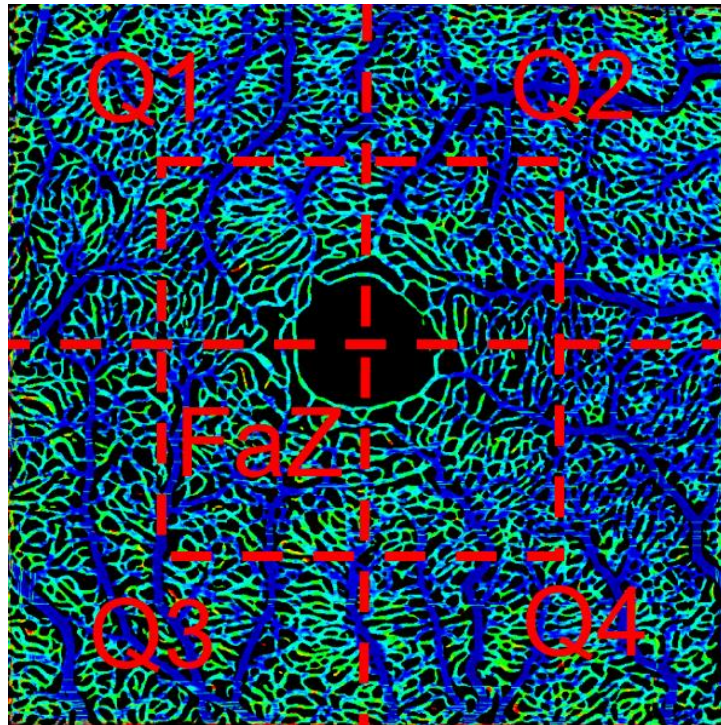


Figure 32: CoV map depicting regions for calculation boundaries.

4.3 CoV Map Comparisons

The CoV maps shown in Sections 4.1 and 4.2 use the method of visualization for the CoV maps described in Section 2.5, while this section uses the method described in Section 3.5. When examining the CoV values in the FAZ region, the maximums for Subjects 1, 2 and 3 are 0.6371, 0.7515, and 0.6889 respectively. The CoV value of 0.7515 was selected and used as the maximum value for the colour range of the CoV maps, as seen in Figure 33 below. The CoV maps shown have a large number of blue vessels due to the limited number of datasets used in this thesis. Processed results with a larger number of datasets may yield a different maximum CoV value and adjust the visualization of the CoV maps accordingly.

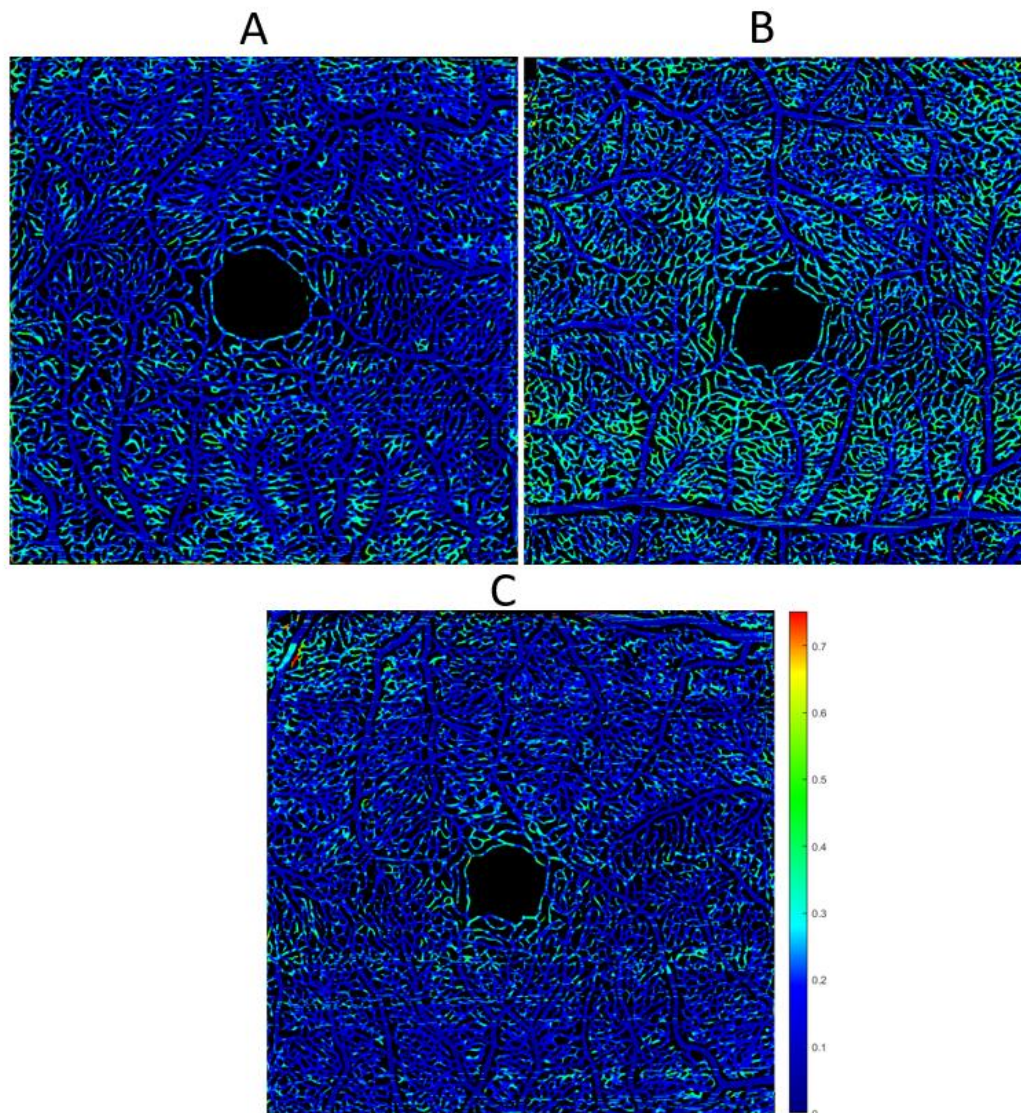


Figure 33: CoV maps of (A) Subject 1, (B) Subject 2 and (C) Subject 3 after bias correction using the visualization method discussed in Section 3.5.

4.4 Summary

This chapter has presented the results of the bias field correction algorithm from three subjects through qualitative examination of the CoV maps and quantitative review of the CoV values. Additionally, an updated method for the visualization of the CoV maps was discussed. Chapter 5 will conclude this thesis with a discussion of the results.

Chapter 5: Conclusion

This chapter will provide a discussion of the results of the bias correction algorithm and conclude with recommendations for future work.

5.1 Discussion

To obtain the most accurate diagnosis, a high standard of image processing must always be met in the medical industry. The registration and averaging algorithm discussed in Chapter 2 was initially implemented on the 2-D Zeiss OCT-A images to generate a high-quality image. Upon review and analysis of the 2-D Zeiss images compared to the images produced from the raw volume data, it was clear that there was preprocessing performed on the 2-D images by the Zeiss device which modified the intensities across the image. These unknown processes make these images unreliable for CoV analysis. The new approach involved putting both the 2-D Zeiss and raw volume produced images through the registration and averaging pipeline. The 2-D images have higher vessel intensities across the image, which allows for higher quality vessel segmentation with the DNN compared to the application of the DNN on the volume produced images. This means that we can use the en-face image generated from the raw volume data for the most accurate intensities, and the DNN mask produced from the 2-D image pipeline result to generate the CoV maps. However, before the 3D images can be processed through the pipeline, they must undergo additional preprocessing of bias field correction.

The bias field intensity nonuniformity present in OCT-A images results in a decreased image quality and can affect subsequent analysis with the images. Correcting the intensity variation is essential as it is not representative of the changes that are occurring with the CoV. The final bias field correction algorithm was produced after an iterative design process, with an overview of this pipeline seen in Figure 25. The results show an increase in CoV of 0.4% for Subject 1 and 0.15% for Subject 3, and a decrease in CoV by 0.72% for Subject 2. These are below the 2% change in CoV that was to be deemed successful after bias field correction. The results are not as expected for the subjects and do not allow us to conclude that the bias field algorithm implemented corrected the intensity variation. However, there are several limitations that need to be addressed for future designs.

5.1 Limitations and Future Work

One limitation of this thesis is that the number of datasets processed is small. This is due to the fact that each dataset is quite large and takes a significant amount of time to process. Applying the developed bias field correction algorithm to a larger number of samples will allow for a more robust evaluation of its success. Additionally, the registration transformations applied to the images are not saved for future use. Any time a modification to the bias field correction algorithm was performed, the images had to be sent through the registration and averaging pipeline again. Future work should include modifying the registration algorithm to store the transformations for each dataset.

A significant limitation in the current bias field correction algorithm is the reliance on an accurate segmentation of the BM boundary. When reviewing the results for several volumes, the segmentation did not accurately follow the layer boundary. Reprocessing of the volumes with modified parameters allowed for a correction of these segmentation inaccuracies. However, this is not a viable solution in the long-term as it requires manual review, a time-consuming process. Future work can involve improving the accuracy of the layer segmentation with the use of a DNN. Another limitation is the requirement for a smoother OCT volume for the input into the Graph-cut segmentation algorithm. Currently in use is a 3-D bounded variance procedure to smooth the OCT volume, but this is time and computationally expensive. Incorporating a simpler filtering method can remedy these issues.

A major future design change to the bias field correction algorithm could be to remove segmentation entirely and estimate the bias fields using the entire OCT volume projection. This approach can be compared to the method described in this thesis to determine if the results produced more uniform intensities across the averaged image.

In conclusion, the algorithm described in this thesis has demonstrated that bias field correction for retinal perfusion heterogeneity analysis did not provide significant changes in the CoV results. Bias field correction has the potential to improve the variation in the OCT-A images but requires further development to provide more reliable results to clinical professionals during the investigation of retinal diseases.

References

- [1] A. K. Schuster, C. Erb, E. M. Hoffmann, T. Dietlein, and N. Pfeiffer, "The Diagnosis and Treatment of Glaucoma," *Deutsches Ärzteblatt International*, 2020.
- [2] K. Allison, D. Patel, and O. Alabi, "Epidemiology of Glaucoma: The Past, Present, and Predictions for the Future," *Cureus*, 2020.
- [3] W. Wang and A. Lo, "Diabetic Retinopathy: Pathophysiology and Treatments," *International Journal of Molecular Sciences*, vol. 19, no. 6, p. 1816, 2018.
- [4] Z. L. Teo, Y.-C. Tham, M. Yu, M. L. Chee, T. H. Rim, N. Cheung, M. M. Bikbov, Y. X. Wang, Y. Tang, Y. Lu, I. Y. Wong, D. S. Ting, G. S. Tan, J. B. Jonas, C. Sabanayagam, T. Y. Wong, and C.-Y. Cheng, "Global Prevalence of Diabetic Retinopathy and Projection of Burden Through 2045," *Ophthalmology*, vol. 128, no. 11, pp. 1580–1591, 2021.
- [5] "Diabetic Retinopathy," Mayo Clinic, 24-Jun-2021. [Online]. Available: <https://www.mayoclinic.org/diseases-conditions/diabetic-retinopathy/symptoms-causes/syc-20371611>. [Accessed: 11-Dec-2022].
- [6] S. Ruia, K. Tripathy, "Fluorescein Angiography," *StatPearls* [Internet]. Treasure Island (FL): StatPearls Publishing; 2022 Aug-22. Available: <https://www.ncbi.nlm.nih.gov/books/NBK576378/>.
- [7] J. Panchapakesan, "Diabetic Retinopathy," Dr Jai Eye Centre, 30-Mar-2017. [Online]. Available: <https://drjai.com.au/diabetic-retinopathy-bundaberg/>. [Accessed: 11-Dec-2022].
- [8] D. Turbert, "What is Optical Coherence Tomography?," *American Academy of Ophthalmology*, 26-May-2022. [Online]. Available: <https://www.aao.org/eye-health/treatments/what-is-optical-coherence-tomography>. [Accessed: 11-Dec-2022].
- [9] J. Walther, M. Gaertner, P. Cimalla, A. Burkhardt, L. Kirsten, S. Meissner, and E. Koch, "Optical Coherence Tomography in Biomedical Research," *Analytical and Bioanalytical Chemistry*, vol. 400, no. 9, pp. 2721–2743, 2011.
- [10] "What is Optical Coherence Tomography (OCT)?," Stoney Creek Eye Care . [Online]. Available: <https://stoneycreekeyecare.com/what-is-optical-coherence-tomography-oct/>. [Accessed: 20-Dec-2022].
- [11] "OCT Ocular Coherence Tomography - 3D scan," Cargills Opticians. [Online]. Available: <https://www.cargillopticians.co.uk/oct-ocular-coherence-tomography-3d-scan/>. [Accessed: 20-Dec-2022].

- [12] T. E. de Carlo, A. Romano, N. K. Waheed, and J. S. Duker, "A Review of Optical Coherence Tomography Angiography (OCTA)," *International Journal of Retina and Vitreous*, vol. 1, no. 1, 2015.
- [13] J. D. Luisi, J. L. Lin, B. T. Ameredes, and M. Motamedi, "Spatial-Temporal Speckle Variance in the En-Face View as a Contrast for Optical Coherence Tomography Angiography (OCTA)," *Sensors*, vol. 22, no. 7, p. 2447, 2022.
- [14] D. Sousa, "Optical Coherence Tomography Angiography," EyeWiki, 09-Jun-2022. [Online]. Available: https://eyewiki.aao.org/Optical_Coherence_Tomography_Angiography. [Accessed: 11-Dec-2022].
- [15] K. G. Falavarjani, J. Khadamy, and K. A. Aghdam, "An Update on Optical Coherence Tomography Angiography in Diabetic Retinopathy," *Journal of Ophthalmic and Vision Research*, vol. 13, no. 4, p. 487, 2018.
- [16] M. Heisler, S. Lee, Z. Mammo, Y. Jian, M. Ju, A. Merkur, E. Navajas, C. Balaratnasingam, M. F. Beg, and M. V. Sarunic, "Strip-Based Registration of Serially Acquired Optical Coherence Tomography Angiography," *J. Biomed. Opt.*, (2017).
- [17] A. Athwal, C. Balaratnasingam, D.-Y. Yu, M. Heisler, M. V. Sarunic, and M. J. Ju, "Optimizing 3D Retinal Vasculature Imaging in Diabetic Retinopathy using Registration and Averaging of OCT-A," *Biomedical Optics Express*, vol. 12, no. 1, p. 553, 2020.
- [18] J. Lo, M. Heisler, V. Vanzan, S. Karst, I. Z. Matovinovic, S. Loncaric, E. V. Navajas, M. F. Beg, and M. V. Šarunic, "Microvasculature Segmentation and Intercapillary Area Quantification of the Deep Vascular Complex using Transfer Learning," *Translational Vision Science & Technology*, vol. 9, no. 2, p. 38, 2020.
- [19] D.-Y. Yu, S. J. Cringle, P. K. Yu, C. Balaratnasingam, A. Mehnert, M. V. Sarunic, D. An, and E.-N. Su, "Retinal Capillary Perfusion: Spatial and Temporal Heterogeneity," *Progress in Retinal and Eye Research*, vol. 70, pp. 23–54, 2019.
- [20] S. Song, Y. Zheng, and Y. He, "A Review of Methods for Bias Correction in Medical Images," *Biomedical Engineering Review*, vol. 3, no. 1, 2017.
- [21] P. Zang, G. Liu, M. Zhang, C. Dongye, J. Wang, A. D. Pechauer, T. S. Hwang, D. J. Wilson, D. Huang, D. Li, and Y. Jia, "Automated Motion Correction using Parallel-Strip Registration for Wide-Field En-Face OCT Angiogram," *Biomedical Optics Express*, vol. 7, no. 7, p. 2823, 2016.
- [22] M. Alam, D. Toslak, J. I. Lim, and X. Yao, "OCT Feature Analysis Guided Artery-vein Differentiation in Octa," *Biomedical Optics Express*, vol. 10, no. 4, p. 2055, 2019.
- [23] N. J. Tustison, B. B. Avants, P. A. Cook, Yuanjie Zheng, A. Egan, P. A. Yushkevich, and J. C. Gee, "N4ITK: Improved N3 Bias Correction," *IEEE Transactions on Medical*

- Imaging, vol. 29, no. 6, pp. 1310–1320, 2010.
- [24] E. Ardizzone, R. Pirrone, O. Gambino, S. Vitabile, "Illumination Correction on Biomedical Images," *Computing and Informatics*. 33. 175-196, 2014.
- [25] W. A. Mustafa, H. Yazid and S. B. Yaacob, "Illumination Correction of Retinal Images using Superimpose Low Pass and Gaussian Filtering," 2015 2nd International Conference on Biomedical Engineering (ICoBE), 2015, pp. 1-4, doi: 10.1109/ICoBE.2015.7235889.
- [26] A. Tatham, "Clinical Advantages of Swept-Source OCT and New Non-Damaging Laser Treatments." *Review of Ophthalmology*, Mar-2014.
- [27] "Plex Elite 9000 Swept-Source OCT Angiography," Swept-Source OCT Angiography. [Online]. Available: <https://www.zeiss.com/meditec/en/products/optical-coherence-tomography-devices/plex-elite-9000-swept-source-oct.html>. [Accessed: 11-Dec-2022].
- [28] "Maestro2 - High Resolution OCT and Color Fundus Photography," Topcon Healthcare | Canada, 22-Jun-2022. [Online]. Available: <https://topconhealthcare.ca/en/products/maestro2/>. [Accessed: 11-Dec-2022].
- [29] R. F. Spaide, J. G. Fujimoto, and N. K. Waheed, "Image Artifacts in Optical Coherence Tomography Angiography," *Retina*, vol. 35, no. 11, pp. 2163–2180, 2015.
- [30] M. Siadati (2022). CoV Quantification for Glaucoma Study [PowerPoint Slides]. Available: <https://drive.google.com/file/d/1gbISC3AYWUJ9PKTJTMYPaB1KWzd9YhDI/view>
- [31] Y. Fu, Y. Lei, T. Wang, W. J. Curran, T. Liu, and X. Yang, "Deep Learning in Medical Image Registration: A Review," *Physics in Medicine & Biology*, vol. 65, no. 20, 2020.
- [32] "Gaussian blur," Wikipedia, 15-Feb-2023. [Online]. Available: https://en.wikipedia.org/wiki/Gaussian_blur. [Accessed: 10-Apr-2023].
- [33] P. M. Shanmugam, V. K. Konana, R. Ramanjulu, and K. C. Divyansh Mishra, "Vitreous Opacities Causing Artifacts in Optical Coherence Tomography Angiography," *Indian Journal of Ophthalmology*, vol. 65, no. 10, p. 1023, 2017.
- [34] A. Camino, Y. Jia, J. Yu, J. Wang, L. Liu, and D. Huang, "Automated Detection of Shadow Artifacts in Optical Coherence Tomography Angiography," *Biomedical Optics Express*, vol. 10, no. 3, p. 1514, 2019.
- [35] S. Lee, N. Fallah, F. Forooghian, A. Ko, K. Pakzad-Vaezi, A. B. Merkur, A. W. Kirker, D. A. Albiani, M. Young, M. V. Sarunic, and M. F. Beg, "Comparative analysis of repeatability of manual and automated choroidal thickness measurements in nonneovascular age-related macular degeneration," *Investigative Ophthalmology & Visual*

Science, vol. 54, no. 4, p. 2864, 2013.

- [36] S. Lee, M. F. Beg, and M. V. Sarunic, "Segmentation of the macular choroid in OCT images acquired at 830nm and 1060nm," SPIE Proceedings, 2013.
- [37] "Know your retinal layers," Know your retinal layers | Heidelberg Engineering. [Online]. Available: <https://business-lounge.heidelbergengineering.com/be/en/news/news/know-your-retinal-layers-33401465>. [Accessed: 10-Apr-2023].